Dynamics of Vortex Interaction and Entrainment Characteristics in Inclined Elliptic Jets using Sparse Track-Enhanced Volumetric Measurements

Xin ZENG[1, 2], Hao QU[1, 2], Chuangxin HE[1, 2]*, Yingzheng LIU[1, 2] & Lian GAN[3]

[1] *Key Laboratory of Education Ministry for Power Machinery and Engineering*

School of Mechanical Engineering, Shanghai Jiao Tong University

800 Dongchuan Road, Shanghai 200240, China

[2] *Gas Turbine Research Institute, Shanghai Jiao Tong University*

800 Dongchuan Road, Shanghai 200240, China

[3] *Department of Engineering, Durham University*
Durham DH1 3LE, UK

* Corresponding author.

E-mail address: chuangxin.he@sjtu.edu.cn (C. He)

Highlights

1. Inclined elliptical jets (incline angles of 30° in major-plane and minor-plane) at aspect ratios (AR) values of 2 under Re = 3,000 were captured by sparse track-enhanced volumetric measurements.
2. The dominant frequencies of the leading and trailing vortex ring for the major-plane inclined-A and minor-plane inclined-B elliptical jet are obtained, and the first axis-switching position of the two inclined jets are indicated.
3. The inclined elliptical nozzles can make the generation of streamwise vortex structures during large-scale vortex structures interaction, enhancing mass entrainment.

Abstract

This work is a further discussion about elliptical jet flows (Zeng et al. Exp. Fluids 64.8, 2023) by exploring how variations in nozzle shape enhance flow control efficiency. The study examines the dynamic evolution of vortex interactions and their positive effects on the entrainment of inclined elliptical jets (with inclination angles of 30° in both the major and minor planes) compared to non-inclined elliptical jets. Experiments were conducted at an aspect ratio (AR) of 2 and a Reynolds number of approximately 3,000. Time-resolved tomographic particle image velocimetry (Tomo-PIV) and three-dimensional Lagrangian particle tracking (3D LPT) measurements were employed to capture the flow dynamics in detail. The Eulerian velocity field datasets obtained from Tomo-PIV are enhanced using high-precision tracks from 3D LPT measurements, improving the accuracy of velocity field reconstruction. Statistical analyses indicate that inclined elliptical jets exhibit greater mass entrainment characteristics and higher momentum flux compared to non-inclined elliptical jets. The power spectral densities (PSDs) and time-domain spectral proper orthogonal decomposition (td-SPOD) results reveal that for the major-plane inclined-A nozzle, both the leading and trailing vortex rings share the same dominant frequency of St = 0.28, suggesting that vortex pairing and merging in the 30° inclined-A jet may be a periodic process. After vortex merging at approximately $Y/D_e \approx 3.5$, the first axis-switching is completed, indicating that axial switching is suppressed in the major-plane inclined-A elliptical jet compared to the non-inclined case. In contrast, for the minor-plane inclined-B jet, the dominant frequencies of the leading and trailing vortex rings are St = 0.28 and St = 0.61, respectively. In some instances, two consecutive large-scale vortex rings corresponding to SPOD mode (3,4) do not merge downstream; instead, they develop independently and eventually break down separately. At the axis-switching plane ($Y/D_e = 2.5$), during both the merging and axis-switching processes of vortex rings in the two inclined nozzles, a significant number of streamwise vortex structures are generated. This phenomenon substantially contributes to an increased mean entrainment rate, further enhancing the mixing characteristics of inclined elliptical jets.

Keywords: Inclined elliptical jet, Tomo-PIV, 3D LPT, Vortical dynamics; Mass entrainment.

1. Introduction

Introducing axial variations in nozzle length along the circumference, known as an indeterminate-origin nozzle, is a cost-effective and efficient passive jet flow control strategy. Examples include inclined elliptical nozzles and other asymmetrical nozzle geometries (New et al. 2015). This approach has been widely applied in industrial and engineering settings, or high-precision machining instruments, significantly enhancing jet mass entrainment rates (Cater and Soria 2002, Quinn 1992) and improving heat transfer efficiency (Bhapkar et al. 2014, He et al. 2015). Although many other geometrical possibilities for an indeterminate-origin nozzle have been investigated (Behrouzi et al. 2017, Kumar et al. 2021, Lim et al. 2018, Lim 1998, Long and New 2016, Wu et al. 2018), inclined nozzles remain of particular interest due to their distinct and well-defined vortex interaction behavior (New, et al. 2015). Inclined elliptical nozzles represent a modification of elliptical jet nozzle geometry, enhancing jet mass entrainment through prevailing azimuthal asymmetry. Their velocity profiles and turbulent flow characteristics have been investigated using planar particle image velocimetry (planar-PIV), while their vortex behavior has been visualized through planar laser-induced fluorescence (PLIF) techniques (New and Tsioli 2014, New and Tsovolos 2011, 2012, 2013), providing qualitative insights into vortex dynamics. While previous studies have provided limited quantitative information on the three-dimensional (3D) velocity field and the interaction of large-scale ring-like vortex structures, a detailed 3D velocity field is essential for investigating the complex vortex dynamics and their interactions, particularly when axis-switching is suppressed in inclined elliptical jets. Advanced tomographic PIV (Tomo-PIV) and 3D Lagrangian particle tracking (3D LPT) (Schröder and Schanz 2022) enable high-resolution 3D velocity field reconstruction, facilitating the 3D coherent structure dynamics and mass transport characteristics in inclined elliptical jets. This is crucial for unveiling underlying flow mechanisms and provides insights into industrial nozzle design strategies, demonstrating that simple modifications to nozzle geometry can lead to more efficient flow control.

The inclined nozzle outlet plane is not perpendicular to the flow direction and is typically fabricated by imposing axial variations in nozzle length circumferentially. These indeterminate-

origin nozzles have been shown to improve scalar transport (Wlezien and Kibens 1986, 1988). While many studies have explored increasingly complex nozzle geometry modifications (Behrouzi, et al. 2017, Kumar, et al. 2021, Lim, et al. 2018, Lim 1998, Long and New 2016, Wu, et al. 2018), inclined nozzles produce relatively well-understood behavior, making them a fundamental research model for studying flow mechanisms and mass transport enhancement strategies. Webster and Longmire (1997) conducted PLIF visualization and planar PIV experiments on inclined circular nozzles under a Reynolds number (Re) of 9,000, with nozzle outlet planes inclined at 0°, 14°, 26°, 37°, and 45°. Their findings showed that as the nozzle tilt angle increased, the jet spread intensified, forming an inclined ring-like vortex (VR). Additionally, the vortex ring gradually moved outward, accompanied by fluid diffusion from within the jet (Webster and Longmire 1998). Troolin and Longmire (2010) further explored the 3D reconstruction of the flow field using time-resolved volume 3-component velocimetry (V3V) (Pereira and Gharib 2002, Pereira et al. 2000) at Re = 2,500 with 14° and 26° inclinations. Their study identified a trailing vortex tube at the tail of the main Kelvin–Helmholtz (K–H) vortex ring, demonstrating that interactions between the trailing vortex structure and the main vortex ring lead to twisting and rotation. For inclined elliptical jets, the New (2009) research group conducted extensive studies using 2D planar-PIV and PLIF visualization techniques (Lim et al. 2020, New and Tsioli 2014, New and Tsovolos 2011, 2012, 2013, New, et al. 2015, Shi and New 2013). Their key findings revealed that the jet flow structure changes significantly when using inclined elliptical nozzles compared to standard elliptical jets. Notably, the axial-switching phenomenon (Hussain and Husain 1989) observed in elliptical jets was found to be suppressed in jets from major-plane inclined-A nozzles, whereas it remained present in jets from minor-plane inclined-B nozzles. Additionally, inclined elliptical nozzles exhibited greater momentum thickness along the inclined direction, resulting in enhanced jet entrainment characteristics. Although previous studies have provided mean velocity distributions, turbulence intensity profiles, and visualizations of vortex ring structures, they have not quantitatively examined the interaction between different vortex structures or the dynamics of these vortex formations. Rao et al. (2020) suggested that the 3D dynamics of elliptical jets and their variants should be investigated using advanced Tomo-PIV techniques for greater accuracy. Furthermore, since entrainment rate calculations require precise vector fields in planes normal

to the jet axis, assessing the entrainment rate using planar-PIV remains challenging. To overcome these limitations, this study employs Tomo-PIV and 3D LPT techniques, which enable direct 3D vortex structure reconstruction, allowing for the monitoring of vortex dynamics and providing quantitative evidence of mass entrainment enhancement. These advanced measurement tools have been selected to offer a more comprehensive understanding of inclined elliptical jet behavior.

The present study builds upon our previous work on elliptic jet flows (Zeng et al. 2023), extending the discussion to explore the complex interactive processes and dynamic properties of vortex structures. This investigation focuses on inclined elliptical jets, comparing them with a non-inclined elliptical nozzle at AR = 2. Experiments were conducted using time-resolved Tomo-PIV and 3D LPT measurements at a Reynolds number of approximately 3,000. The study specifically examines jets inclined at 30° in the major and minor planes, which exhibit distinct differences from those produced by non-inclined nozzles (New and Tsovolos 2011). The displacement fields of the inclined elliptical jets were reconstructed using a GPU-accelerated Tomo-PIV framework (Zeng et al. 2022), developed based on CPU-based Tomo-PIV codes (Gan et al. 2012, Worth 2010). The long tracks of tracer particles were captured using a 3D LPT framework, referred to as the line-of-sight constraints LPT (LOSC-LPT) framework (Zeng et al. 2024). The Eulerian velocity fields obtained from Tomo-PIV were further enhanced using the high-precision tracks from 3D LPT measurements, employing the sparse track-enhanced volumetric reconstruction strategy. Subsequently, the Eulerian velocity field datasets were analyzed using time-domain spectral proper orthogonal decomposition (td-SPOD) to identify multi-dominant coherent structures, capture the temporal evolution of coherent structures, and examine the dynamics of vortex interactions. Additionally, the mass entrainment of the inclined elliptical jets was quantitatively evaluated using high-precision Eulerian velocity fields, providing deeper insights into their entrainment characteristics.

The remainder of this paper is structured as follows. Section 2 presents the methodological framework, including the experimental setup (Section 2.1), 3D flow field reconstruction techniques for data acquisition and processing (Section 2.2), and the time-domain spectral

proper orthogonal decomposition (td-SPOD) method for vortex dynamics analysis (Section 2.3). Section 3 provides an in-depth discussion of four critical aspects of inclined elliptical jets: the accuracy assessment of reconstructed flow fields for measurement validation (Section 3.1), statistical characterization of flow features (Section 3.2), vortex interaction dynamics (Section 3.3), and mass entrainment enhancement mechanisms (Section 3.4). Finally, Section 4 summarizes the key findings and contributions of this study.

2. Methodology

2.1 Experimental Setup

All the experiments were conducted in an octagonal tank (with sides of 250 mm and a height of 900 mm), as shown in Fig. 1(a) (He et al. 2021, He et al. 2022). The jet behavior under different geometries can be measured thanks to the deformable nozzle outlet installation of the tank, and the flow rate can be controlled precisely by a frequency-conversion pump. A stabilizing chamber with a honeycomb filter was designed at the bottom of the tank to obtain a steady jet flow. The exit of different nozzles extended into the tank for approximately 210 mm to reduce the effect of the wall on the flow field. This study used an elliptic nozzle of AR = 2 and its two geometric varieties, all with an equivalent diameter D_e = 20 mm, the equivalent diameter D_e was defined as the diameter of a circular jet with a momentum flux equal to that of an elliptic jet of exit semi-major and semi-minor axes a and b respectively, i.e. $D_e \equiv 2(ab)^{1/2}$ (Hussain and Husain 1989), the Re is about 3,000 according to the equivalent diameter and flow velocity U_0. The design and manufacturing of inclined elliptic nozzles referred to the work by Hussain and Husain (1989), with a contraction ratio from a circular to an elliptic cross-section and the contraction profile of elliptic nozzles follows a third-order polynomial curve with short straight portions on both upstream and downstream ends, which are displayed in Fig. 1(c–d). As shown in Fig. 1(e–h), two types of inclined nozzles were inclined along the major plane and the minor plane, and the incline angles are all set as 30°, which is cut directly from the elliptic nozzle of AR = 2 for the direct comparison in entrainment enhancement, all the details of nozzles are all displayed in Table 1. And further details of the experimental setup can be found in the literature (He, et al. 2021, He, et al. 2022).

Table 1 Geometries of nozzles used

Nozzle	a (mm)	b (mm)	D_e (mm)	L_u (mm)	L_n (mm)	L_d (mm)
elliptic	14.14	7.07	20	20	160	30
major-plane inclined-A	14.14	7.07	20	20	160	30
minor-plane inclined-B	14.14	7.07	20	20	160	30

The tank is filled with tap water, meanwhile inside the fluid was seeded with 50-μm polyamide tracer particles (Dantec, Denmark). The volumetric light was produced by a 25-W continuous-wave laser operating at 532 nm (Millennia EV25S, USA), which was expanded to a cylinder with a diameter of 50 mm. The particle images were captured in the continuous acquisition mode with a sampling rate of 1,000 image pairs per second by two 12-bit complementary metal–oxide–semiconductor cameras (PCO, Germany) with an image resolution of 2,000 × 2,000 pixels. The average particle size in the image was 3 × 3 pixels and the particle density in the image was approximately 0.02 particles per pixel. Each image will be divided into two views owing to the use of mirrors, as shown by the red dashed line for the top view of the two cameras and their relative positions in Fig. 1(a). This strategy of a combination of prismatic and planar mirrors meant that only two cameras were required (Bardet et al. 2010) to obtain four different views with a resolution of 1,000 × 2,000 pixels.

The 3D displacement fields near the exit of the inclined elliptical nozzles were reconstructed by time-resolved Tomo-PIV and 3D Lagrangian Particle Tracking (3D LPT) techniques. The 3D volumetric calibration of each camera was calibrated using a checkerboard calibration plate with a mesh spacing of 5 mm, and a 30-mm (±15 mm) normal shift of the calibration plate was achieved through a traversal mechanism. The reconstructed area was 50 mm (2.5D in the X-direction) × 100 mm (5D in the Y-direction) × 50 mm (2.5D in the Z-direction), as shown by the reconstructed volume in Fig. 1, where, the X-direction is along the major axis, Z-direction is along the minor axis of the elliptical nozzle, Y-direction is downstream of the jet. For the Tomo-PIV reconstruction, the discretization level was set as 11 voxels/mm to obtain the particle field, and the velocity vectors were calculated efficiently using a graphics processing unit (GPU)-based Tomo-PIV framework developed in-house (Zeng, et al. 2022), which was developed based on the CPU Tomo-PIV code(s) (Gan, et al. 2012, Worth 2010). The interrogation volume during the 3D cross-correlation was set in turn to 64^3 and 32^3 voxels with a 50% overlap, which realized a resolution of 14 vectors per D_e, each vector field can be recovered in 2.05 minutes with the GPU (NVIDIA Tesla V100S, 32GB). For 3D LPT, the long trajectories of tracer particles were reconstructed by the LOSC-LPT framework (Zeng, et al.

2024). The LOSC-LPT framework was an improvement of the “Shake-The-Box (STB)” (Schanz et al. 2016) technique using the polynomial calibration model and the line-of-sight constraints (LOSC) to overcome the refractive interface issues in LPT measurement. It draws inspiration from the two-plane polynomial camera calibration in Tomo-PIV (Worth 2010) and the STB-based open-source Lagrangian particle tracking (OpenLPT) framework (Tan et al. 2020). The use of polynomial mapping results in smaller mean calibration error of less than 0.1 px for the measurements in the presence of refractive interfaces. For the LOSC-LPT technique, the number of iterative particle reconstruction (IPR) (Wieneke 2013) iterations is set to 4, the number of dithers in the IPR and STB is set to 6, the initial dither width is set to 2.0 px, as well as the allowable 3D reconstruction error is set to 0.8 px, the mean IPR time per frame of particles cloud is 1.67 minutes with CPU (Intel® Xeon® Gold 6230, 40 cores). The measurements of each nozzle were repeated 2 times with 6,320 image sets recorded each time, which can offer 6320 frames of 3D flow-field snapshots for each jet.

2.2 Sparse track-enhanced volumetric reconstruction

In the experiments of inclined elliptical jets, although the polynomial camera model is applied, Fig. 2 demonstrates that after volume self-calibration (VSC) (Wieneke 2008), the mean calibration errors for the four views are still 0.07 px, 0.11 px, 0.22 px, and 0.08 px, respectively. The higher camera calibration errors for views 2 and 3 may be caused by the blurring of the tank wall or the loss of the camera CMOS chip and lens. The higher errors indicate that this dataset is amenable to data processing using the Tomo-PIV framework (calibration error < 0.4 px (Elsinga et al. 2006)) while not suitable for processing using the 3D LPT technique (calibration error < 0.1 px (Wieneke 2008)). However, the higher calibration error can well simulate more complex situations that may be encountered in real engineering applications, such as the presence of irregularly curved refractive walls or other causes of image blurring in the captured area, resulting in a reduced number of high-precision particle tracks reconstructed by 3D LPT, and preventing the reconstruction of higher spatial resolution 3D flow field from the Lagrangian tracks. Figures 3(a-i, ii) show the instantaneous velocity fields of two inclined elliptical jets reconstructed by Tomo-PIV, with the vortex structure visualized by an iso-surface

with Q criterion (Jeong and Hussain 1995) as 0.5 U_0^2/D_e^2. The sliced contour maps of the velocity distribution at $X/D_e = 0$ on the minor axis of the elliptical jets are colored according to the local divergence of velocity. Notably, the flow-field noise is large, and the non-zero divergence of velocity is significant (most absolute values greater than 1.0 U_0/D_e^2) in the Tomo-PIV data.

Figures 3(b-i, ii) present the particle tracks obtained via 3D LPT, depicting 200 successive time steps with tracks color-coded by streamwise velocity. Due to significant calibration errors, the number of 3D LPT particle tracks is relatively low, with 5,823 noisy tracks for the major-plane inclined-A (mean deviation: 0.047 px, defined as the mean deviation between the original tracks and the fitted tracks after applying the TrackFit method (Gesemann et al. 2016) and only 3,524 noisy tracks for the minor-plane inclined-B (mean deviation: 0.052 px). Despite the noise, 3D LPT (Schanz, et al. 2016) is generally recognized for its higher accuracy compared to the voxel-based Tomo-PIV method (Elsinga, et al. 2006). A common approach for post-processing and visualization involves transporting the 3D LPT tracks onto an Eulerian vector field, facilitating broader data analysis operations. Gesemann, et al. (2016) introduced the FlowFit method, which represents the velocity at particle positions, $\boldsymbol{u}_{\text{p, LPT}}$ or grid nodes $\boldsymbol{u}_{\text{grid, LPT}}$, as a weighted linear combination of surrounding Eulerian velocity field grid points using radial basis functions (RBF). The cost function is then formulated by comparing the velocity $\boldsymbol{u}_{\text{p, LPT}}$ at measured points from 3D LPT with the fitted velocity $\boldsymbol{u}_{\text{p, fit}}$ incorporating velocity divergence constraints and the gradient of divergence as L_2 regularization terms. This formulation is referred to as the FlowFit-Div1 version (Gesemann, et al. 2016),

$$\begin{aligned} &\min L : \left\| \boldsymbol{u}_{\text{p,LPT}} - \boldsymbol{u}_{\text{p,fit}} \right\|_2^2 + \eta_i \left\| R_i \right\|_2^2 \\ &R_1 := \nabla \cdot \boldsymbol{u}_{\text{grid}}, i, j, k \in \Gamma \\ &R_2 := \nabla(\nabla \cdot \boldsymbol{u}_{\text{grid}}), i, j, k \in \Gamma \end{aligned} \quad , \tag{1}$$

where, $\boldsymbol{\Gamma}$ represents all grid nodes, while η_i denotes the regularization coefficient, which is adjusted based on the grid size to prevent gradient explosion during optimization. The FlowFit-Div1 method is typically applied with a grid point-to-particle ratio of approximately 10:1, meaning that each particle is surrounded by more than 10 grid points (Gesemann 2018). For

velocity field reconstruction with sparse tracks, the limited number of tracks reduces the precision and efficiency of FlowFit. To address this issue, acceleration at particle positions can be incorporated as an L_1 regularization term, alongside the incompressible Navier-Stokes (N-S) equation. This formulation strengthens the coupling between velocity and pressure, defining the FlowFit-Div2 version (Gesemann, et al. 2016). However, enforcing the N-S equation constraint transforms the cost function into a nonlinear least squares problem, significantly increasing computational complexity. When dealing with a large number of grid nodes, gradient calculations through differentiation become highly intricate and inefficient.

To enhance the accuracy of volumetric flow field reconstruction, we propose a sparse track-enhanced strategy based on FlowFit-Div1 (Gesemann, et al. 2016) This approach improves data quality by reducing errors and noise in the Tomo-PIV dataset, facilitating flow-field filtering and outlier correction (OC). As illustrated in Fig.4, the reconstruction process consists of two key steps. In Step I (Fig.4(a→b)), the instantaneous velocity field obtained from Tomo-PIV serves as the initial estimate of the velocity field on the grid. In Step II (Fig.4(c→b)), high-precision velocity information from sparse 3D LPT particle tracks is used to refine the Tomo-PIV flow field at corresponding time steps. To mitigate the high grid point-to-particle ratio, velocity vectors at grid nodes in the Tomo-PIV field are treated as virtual particles, thereby avoiding the need to incorporate the N-S equation. This prevents the cost function in Eq. (1) from becoming nonlinear, allowing for efficient optimization without the computational overhead of automatic differentiation. A detailed summary of computational time will be provided in Section 3.1 for the experimental data, following the validation of 3D reconstruction accuracy. This summary will include the total processing time for single-frame flow field reconstruction, incorporating both Tomo-PIV and 3D LPT. Additionally, particle acceleration is excluded from the optimization, as acceleration data typically contains high errors. Following the sparse track-enhanced data refinement (Fig.4(b→e)), the error and noise in each instantaneous Tomo-PIV flow field are significantly reduced. As a result, large-scale structures are expected to become more dominant in the reconstructed velocity field, while missing small-scale structures can be effectively recovered.

2.3 Spectral proper orthogonal decomposition

After the sparse track-enhanced volumetric reconstruction, the massive velocity field data of jet flows still contains high noise, which can be resolved by the mode decomposition method, such as the classical Fourier decomposition, proper orthogonal decomposition (POD) (Lumley 1967) or its variants (Sirovich 1987, Wall et al. 2003), dynamic mode decomposition (DMD) (Rowley et al. 2009, Schmid 2010), and recently time domain spectral proper orthogonal decomposition (td-SPOD) (Sieber et al. 2016), extracting the large-scale flow structures from turbulent flow fields and monitoring flow behavior. For the presented time-resolved noised measurements by Tomo-PIV and sparse track-enhanced volumetric reconstruction strategy with Tomo-PIV and 3D LPT, the td-SPOD is selected for investigating coherent structure interactions and their time-dynamic evolution, which is suitable for investigating mode interactions between various wavelengths and the time-dynamic evolution of modes, rather than the classical frequency-domain spectral proper orthogonal decomposition (fd-SPOD, classical SPOD) (Towne et al. 2018), which was mainly applied to extract unknown coherent structures according to frequencies (Karami and Soria 2018, Schmidt et al. 2018). The td-SPOD algorithm was developed from classical POD, and more detailed information on the identification of dominant structure in the flow field by td-SPOD can be found in the work by Sieber, et al. (2016).

3. Results and discussions

3.1 Accuracy of sparse track-enhanced volumetric reconstruction

The data in the schematic diagram of Fig. 4 is a validation for the sparse track-enhanced volumetric reconstruction strategy based on the Johns Hopkins DNS Turbulence database (JHTDB) (Li et al. 2008) with a grid of 32^3, the number of particles is 4,000. After modifying the Tomo-PIV flow field with 4,000 particles, Figure 4(e) displays the vortex structure in the *Q* criterion as 120 [-], which is almost completely reconstructed with high accuracy compared to the DNS reference (Fig. 4(d)). Figures 5(a–d) presents the DNS reference flow field alongside the reconstructed flow fields obtained using Tomo-PIV, FlowFit + 4,000 particles, and Tomo-PIV + 4,000 particles. The flow field reconstructed solely from 4,000 particle tracks fails to accurately reproduce the velocity distribution in critical regions, and flow details are not well preserved. This suggests that FlowFit-Div1 requires sufficient particle velocity data to effectively reconstruct the original velocity field. While the Tomo-PIV reconstruction captures the main large-scale structures of the flow, it lacks finer details. In contrast, the Tomo-PIV + 4,000 particles reconstruction achieves higher accuracy, effectively preserving intricate flow details and faithfully reproducing all structures within the flow field. A quantitative evaluation of velocity field reconstruction in different modes is presented in Fig. 5(e) and its localized zoom-in view in Fig. 5(f). The velocity *U* data is extracted along the *Y*-axis within the range [-20 mm, 20 mm], with *X* and *Z* set to 0 mm. The FlowFit + 4,000 particles velocity *U* deviates more from the DNS reference flow field in the localized *Y*-axis range [-10 mm, -5 mm], primarily due to a lower particle count in this region. The velocity *U* deviation from the DNS baseline velocities is larger for Tomo-PIV alone, but with the correction of 4,000 particles, the Tomo-PIV + 4,000 particles reconstruction produces velocity *U* values closer to the DNS baseline, with an overall average absolute error of 0.0552 m/s (average relative error of 2.40%). This error is smaller than that by FlowFit + 4,000 particles reconstruction, which has an error of 0.0992 m/s (4.31%).

For the experimental datasets of inclined elliptical jets, Figure 3(c-i) illustrates that for the major-plane inclined elliptical jet, the first large-scale vortex ring near the nozzle exit is clearly identified, benefiting from the high number of particle trajectories. However, the overall flow field noise remains significant, and the sliced contour maps of velocity dispersion exhibit higher values, primarily due to the velocity zero-dispersion constraint introduced by FlowFit. For the minor-plane inclined elliptical jet, the 3D flow field reconstructed directly from 3D LPT struggles to accurately capture vortex structures, showing a high level of noise compared to Tomo-PIV results from Figure 3(c-ii). In certain regions, velocity scattering contour maps reveal strong localized peaks, further indicating that the accuracy of the 3D flow field reconstruction from 3D LPT alone is low, making it unsuitable for further analysis. With the sparse track-enhanced volumetric reconstruction strategy using Tomo-PIV and 3D LPT, the velocity fields by the Tomo-PIV technique have been corrected and become more accurate, which recovers more complete coherent structures in Figs. 3(d-i, ii). Statistical analysis was conducted on the velocity divergence values in the region of $r/D_e < 1.0$ (r is the radial coordinate defined as $r = \sqrt{x^2+z^2}$) in the instantaneous velocity field. As shown in Figs. 6(a, c), for both inclined elliptical jets in the original Tomo-PIV results, many values of the absolute divergence are over 1.0 U_0/D_e. With the sparse track-enhanced volumetric reconstruction strategy, the values of the absolute divergence are reduced to less than 1.0 U_0/D_e. The noises in the flow field are reduced and the overall divergence of velocity is much closer to 0 compared with the original Tomo-PIV, which is a sign that speed continuity is satisfied and indicates that the data enhancement strategy has a higher accuracy.

The correctness of the sparse track-enhanced volumetric reconstruction can be also verified by plotting the velocity gradient tensor invariants Q^* and R^* to further analyze the turbulence statistical features of the velocity field reconstruction (Das and Girimaji 2022). The zero-discriminant lines are determined according to $Q^{*3} + 27R^{*2}/4 = 0$. The joint Probability Density Functions (joint PDFs) of the second and third invariants (R^*–Q^*) characterize the frequency of occurrence of various localized flow topologies. In various turbulence joint PDFs, the vortex energy-proposed vortex energy generation quadrant ($R^* < 0$ and $Q^* > 0$) and the

dissipation-dissipation generation quadrant ($R^* > 0$ and $Q^* < 0$) should be dominant, exhibiting the characteristic teardrop shape Vieillefosse (1984) with a higher probability of occurrence along the right-hand discriminant. Figs. 6(b, d) show the distribution of R^*–Q^* joint PDFs of all the instantaneous velocity fields before (purple contour map) and after corrections (red contour line) by sparse track-enhanced volumetric reconstruction. Both the pre- (purple contour map) and post-correction (red contour line) velocity fields maintain the higher probability distribution along the discriminant, preserving the teardrop-shaped joint PDF characteristic of turbulent velocity fields, and the PDF in the zone of ($R^* > 0$ and $Q^* < 0$) are slightly compressed, preserving the turbulence features of the flow field, and indicating better velocity field reconstruction results by sparse track-enhanced volumetric reconstruction.

The calibration errors for one or two of the multi-views are high in Tomo-PIV or 3D LPT, which are very common in real experiments and engineering flow control, such as the presence of irregularly curved refractive walls or other unknown causes of image blurring in the captured area, resulting in the reconstruction of exact 3D flow field from the Lagrangian tracks fails. What's more, In terms of efficiency, in Steps I (Fig. 4(a)) and II (Fig. 4(b)) of the sparse track-enhanced volumetric reconstruction algorithm, the original Tomo-PIV velocity field was corrected by 3D LPT tracks, the average time for each frame of vector field in 36 × 70 × 36 vectors was 0.54 minutes with CPU(Intel® Xeon® Gold 6230, 40 cores). By the data fusion of Tomo-PIV (2.05 minutes) and 3D LPT (1.67 minutes), a frame of accurate 3D flow field with grid nodes of 36 × 70 × 36 can be obtained in 2.59 (2.05 + 0.54) minutes (Tomo-PIV and 3D LPT can be conducted concurrently), in a high efficiency. The sparse track-enhanced volumetric reconstruction strategy is a way to utilize the advantages of the Tomo-PIV and 3D LPT techniques, obtaining high-accuracy vector field reconstruction efficiently, which is significant for imperfect practical 3D experiments and complex engineering applications.

3.2 Statistical analysis

Following the sparse track-enhanced volumetric reconstruction using Tomo-PIV and 3D LPT, measurement accuracy is evaluated based on flow continuity in the incompressible flow

regime and the assumption of a uniform random error distribution in each velocity component under ideal conditions. Specifically, the random velocity errors $\delta(U)$ and the relative uncertainty of the mean flow are used as key metrics (Atkinson et al. 2011, Scarano et al. 2006). Table 2 summarizes the measurement uncertainties of the vector fields, comparing the original Tomo-PIV results with those obtained after sparse track-enhanced volumetric reconstruction. The maximum random uncertainty ($\delta(U)/U_0$) values of 4.39%, and the mean relative uncertainty of the mean flow at 0.40% in the Tomo-PIV results are reduced to 3.36% and 3.32%, respectively, after applying the reconstruction across three nozzles. For Reynolds stress, the mean relative uncertainties after sparse track-enhanced volumetric reconstruction do not exceed 6.42%, 5.97%, and 6.47% for the three nozzles, respectively. These low random velocity errors and relative uncertainties indicate that the sparse track-enhanced volumetric reconstruction achieves high precision in flow field reconstruction.

Table 2 Measurement uncertainty of vector fields

	Original Tomo-PIV			After sparse track-enhanced		
	elliptic	major-plane inclined-A	minor-plane inclined-B	elliptic	major-plane inclined-A	minor-plane inclined-B
$\delta(U)/U_0$	4.39%	4.11%	4.29%	3.36%	3.32%	3.22%
$\delta_{\overline{U}}$	0.39%	0.37%	0.40%	0.34%	0.35%	0.32%
$\delta_{\overline{U_iU_j}}$	7.72%	6.82%	6.89%	6.42%	5.97%	6.47%

Figure 7 presents the mean velocity field cross-sections in both the major and minor planes for different jets. In the reference elliptical nozzles with an aspect ratio (AR) of 2, the velocity field distributions vary between the major and minor planes. Some asymmetries in velocity fluctuation can be attributed to the particle reconstruction errors in regions farther from the camera's line of sight or limited number of flow field samples. In the minor-plane cross-section ($Z = 0$), the jet expands monotonically, as shown in (Figs. 7(c, e)), resembling a circular jet but with a higher velocity. The mean velocity field distributions for the major-plane inclined-A and minor-plane inclined-B elliptical jets are similar to those of the non-inclined elliptical jet nozzle, exhibiting a characteristic top-hat distribution. The velocity distribution of the major-plane inclined-A jet reveals that its jet core is deflected in the $+X$ direction, as observed in Figs. 7(c). Meanwhile, for the minor-plane inclined-B jet, the jet core is deflected in the $+Z$ direction, as

seen in Figs. 7(f). The mean velocity fields indicate that the jet core deviates from the axial direction of the elliptical nozzle and instead aligns with the nozzle outlet's normal direction. However, the deflection angles remain significantly smaller than 30°. Specifically, the inclined-A jet exhibits a deflection angle of 2.42°, while the inclined-B jet has an angle of 2.51°. This relatively small deflection is likely attributed to the higher flow velocity. The time-averaged field of the inclined elliptical jet further demonstrates a deflection characteristic aligned with the normal direction of the inclined plane. The orientation of the inclined plane plays a crucial role in determining the degree of deflection, while flow velocity also influences the extent of this deviation. These findings provide valuable insights for the design of flow control systems that leverage inclined elliptical jets for improved aerodynamic performance. The stronger velocity fluctuation appears in the axis direction of the nozzle's edges for each jet, and the profile distribution shows the same inclined trend as the velocity distribution in two inclined elliptical jets. The velocity fluctuation profiles of the major-plane inclined-A jet deflected in the $+X$ direction, meanwhile, for the minor-plane inclined-B jet, the profiles deflected in the $+Z$ direction, and the deflection angle have not been quantified due to measurement errors, which has a little influence on the analysis of the large-scale flow structure in the later sections.

The entrainment rate and momentum flux are quantitatively assessed in Fig. 8, with variations in the volume flux J/J_0 (J_0 is the volume flux leaving the non-inclined elliptical nozzle with velocity U_0) and M/M_0 (M_0 represents the initial momentum flux from the nozzle) occurring along the streamwise direction. Fig. 8(a) shows the increase of volume flux at the exit of nozzles in the range $0 < Y/D_e < 1.0$, which may not be quite accurate due to the geometric occlusion due to the inclined top section. The most concerned area is the range $1.0 < Y/D_e < 4.0$ of axis-switching events in elliptical jet and its variants under AR = 2 because the non-inclined elliptical jet shows better entrainment compared with the circular jet (Zeng, et al. 2023). The momentum flux can describe the jet's mixing characteristics, calculated by (Hussein et al. 1994),

$$M(Y) = \rho \iint [U^2 + u'^2 - \frac{1}{2}(v'^2 + w'^2)] dX dZ, M_0 = \frac{\pi^3 \rho U_0^2 D_e^2}{16}, \quad (8)$$

where M_0 is the initial momentum flux from the nozzle exit, and all the momentum fluxes are normalized by M_0. Figure 8(b) reveals the results for all the cases, in the zone of $1.0 < Y/D_e <$

4.0, all the momentum fluxes of jets decrease with the downstream evolution, while the inclined elliptical jets indicate larger momentum fluxes. The greater momentum fluxes in inclined elliptical jets represent stronger mixing characteristics and momentum transportation performance, which provide evidence for the higher entrainment rate from Fig. 8(a). The mass entrainment characteristics will be further discussed in Section 3.4 quantitatively with the spatial derivative of the volume flux.

3.3 Coherent Structure Extraction and Vortex Dynamics

The dominant frequencies of the flow structures are detected by the power spectral densities (PSDs) of the axial Y velocity component in the Y-axis along the centerline from Fig. 9. For td-SPOD in this work, the filter width N_f for filter coefficients vector $\boldsymbol{g}_k$ was set to two periods of large-scale vortex ring, as $N_f = 256 \approx 2f_{\mathrm{PIV}}/f_n$, and the size of $\boldsymbol{g}_k$ was 513 frames. Therefore, all the PSDs were computed using a window shift with 512 time-series data in each window and an overlap rate of 80%, the window size being almost equal to the size of $\boldsymbol{g}_k$ in td-SPOD. A prominent peak Strouhal number ($\mathrm{St} = f \times D_e/U_0$), St = 0.39, is observed in Fig. 9(a) for the non-inclined elliptical jet, indicating the coexistence of multiple large-scale Kelvin–Helmholtz (K–H) ring-like vortex structures propagating in the axial direction. For the major-plane inclined-A nozzle, Figure 9(b) shows a distinct spectral peak at St = 0.28, accompanied by a broadband spectral distribution in the downstream region. Similarly, for the minor-plane inclined-B nozzle, Figure 9(c) also exhibits a pronounced peak at St = 0.28 at $Y/D_e = 3.0$. These spectral peaks may be associated with the formation of single- or multi-scale vortex rings generated at the nozzle exit. These PSD results effectively capture the dominant structural frequencies in the flow field. However, they do not provide direct information about the specific structures associated with these frequencies. To address this, the SPOD algorithm is employed to extract coherent structures and analyze their vortex dynamics in both non-inclined and inclined elliptical jet flows, offering deeper insights into their behavior and evolution.

The td-SPOD method provided a way for identifying the linked modes with the same spectral content and a fixed phase difference of $\pm\pi/2$, the linked modes represent dominant

energetic coherent structures, meanwhile, the dynamic behavior of single dominant coherent structures in the flow can be monitored by reconstructing the linked mode pairs. Td-SPOD can find the associated energy contribution K (defined as $(\lambda_i + \lambda_j)/\sum \lambda_k$) of the mode pairs (Sieber, et al. 2016), as well as the dominant frequency of each linked mode pair. Figures 10(a-i, b-i, c-i) displayed the energy contribution of all mode pairs obtained by td-SPOD, where the diameter and color of the circle indicate the harmonic correlation (harmonic correlation quantifies the spectral proximity between a pair of conjugate modes representing a single coherent structure). The horizontal labels of "linked mode pair labels" are ordered based on declining harmonic correlation, and the four mode pairs with the highest correlation are then sequentially reordered and renumbered 1-4 according to their decreasing energy, where the two most energetic mode pairs will be further discussed in detail. Note that the most correlated pair of modes (the darkest color) does not necessarily correspond to the highest energy (Sieber, et al. 2016).

For the reference elliptical jet flow field at an aspect ratio (AR) of 2, the energy percentages of the first and second pairs of linked modes are 10.96% and 6.52%, respectively, as shown in Fig. 10(a-i). The power spectral densities (PSDs) of the time coefficients for these mode pairs (Figs. 10(a-ii, iii)) reveal that the dominant frequency of the leading elliptical Kelvin–Helmholtz (K–H) vortex ring, corresponding to the linked mode pair (1,2), is St = 0.39. Meanwhile, the trailing elliptical K–H vortex ring, associated with the linked mode pair (3,4), has a lower frequency of St = 0.28. Both frequencies are characteristic of the K–H instability. Since the frequency St = 0.28 of the trailing vortex rings (mode pair (3,4)) is lower than the St = 0.39 of the leading vortex rings (mode pair (1,2)), vortex pairing and merging in the elliptical jet at AR = 2 is not a continuous process, a phenomenon previously confirmed by Zeng, et al. (2023). The spatial structures of these two mode pairs at AR = 2 are visualized in Fig. 11 using the Q-criterion as $Q = 10\ U_0^2/D^2$, illustrating the evolution of spatial structures along the axial direction. The most energetic linked mode pairs (1,2) and (3,4) correspond to elliptical ring-like structures generated in the initial shear layer of the jet. As depicted in Figs. 11(c, d) with $Q = 0.5\ U_0^2/D^2$ from two instantaneous fields, a sequence of elliptical vortex rings forms, rolling up into vortices that grow as they entrain ambient fluid, these instantaneous fields were selected

after the modal analysis, aiming to find clear evidence of the flow structures associated with specific modes in the raw measured data. Before breakdown occurs, the vortex rings expand downstream, with their diameters nearly spanning the entire jet radius. The merging of vortex rings downstream at $Y/D_e \approx 1.8$, as previously observed for elliptical jets by Husain and Hussain (1991), is illustrated in . The merger of two elliptical vortex rings predominantly occurs in the major plane due to the differential expansion of the leading and trailing vortex rings. Specifically, the leading vortex ring expands more in the minor plane than the trailing vortex ring, while their expansion in the major plane remains consistent. During the pairing and merging process, the shape of the elliptical vortex rings continuously changes, leading to an interchange of the original major and minor axes—a phenomenon known as axis-switching (Shi et al. 2019). The merged ring-like structures undergo axis-switching at approximately $Y/D_e \approx$ 2.5 (Zeng, et al. 2023).

For the major-plane inclined-A elliptical nozzle, Figure 10(b-i) shows that the energy percentages of the first and second pairs of linked modes are 9.21% and 5.40%, respectively, both lower than those of the non-inclined elliptical jet. The power spectral densities (PSDs) of the time coefficients for the first two mode pairs (Figs. 10(b-ii, iii)) indicate that both mode pairs (1,2) and (3,4) share the same dominant frequency of St = 0.28, consistent with the PSDs of the axial Y velocity component in Fig. 9(b). This suggests that the pairing and merging of vortex rings may occur as a periodic process. The spatial structures of these two mode pairs, along with the instantaneous structures of the inclined elliptical vortex rings at two moments within one cycle, are visualized in Fig. 12 using the Q-criterion. The most energetic linked mode pairs (1,2) and (3,4) correspond to inclined elliptical ring-like vortical structures in Figs. 12(a, b). As shown in Figs. 12(c, d) of two instantaneous flow fields, the criterion for selecting the instantaneous flow fields at these two moments was their ability to capture the two vortex ring structures associated with the highest-energy mode pairs, as well as the upcoming vortex ring interactions. In Figs. 12(c, d), multiple large-scale ring-like vortex structures are present, with the initial vortex ring forming near the nozzle exit. As the flow evolves downstream, the lower end of the vortex ring moves faster, curling upward slightly. Subsequently, two adjacent large-scale vortex rings undergo pairing and merging processes as they convect downstream.

The large-scale vortex ring dynamics are further visualized in Fig. 13 which clearly illustrates the merging process of the leading vortex ring (VR1) and trailing vortex ring (VR2) across eight key moments in a complete cycle. The instantaneous field in Fig. 12(c) corresponds to the reconstructed flow field in Fig. 13(b) (t/T = 0.125), where the two vortex loops have fully formed at the nozzle exit and have evolved downstream. The instantaneous field in Fig. R3(d) corresponds to the reconstructed flow field in Fig. 13(e) (t/T = 0.50), at which point the two vortex rings begin pairing and are about to merge in the subsequent moment (t/T = 0.625). And the different vortex structures can be divided by comparing the vortex structures in the reconstructed flow field of both mode pairs with those in the flow field reconstructed using only a single mode pair. The merging process begins when VR1 exits the nozzle, while VR2 emerges at the nozzle exit. Compared to the non-inclined elliptical jet, the merging location in the major-plane inclined-A elliptical jet differs slightly, occurring near the end of the long axis of the vortex ring in the $-X$ direction (the higher end of the inclined nozzle), as seen in Fig. 13(f). The merging initiates at approximately [$X/D_e \approx$ -0.5, $Y/D_e \approx 2.0$, $Z/D_e \approx \pm 0.3$]. During this process, VR2 transitions into a vortex tube at the end of VR1 (Figs. 13(f, g)) Subsequently, the towed vortex tube may develop into a streamwise vortex structure, enhancing mass entrainment. Following the merger, the combined vortex rings deform and undergo axis-switching due to self-induction as the jet develops axially. However, in the major-plane inclined-A elliptical jet, the first axis-switching occurs further downstream at $Y/D_e \approx 3.5$, compared to $Y/D_e \approx 2.5$ in the non-inclined elliptical jet. This shift suggests that axis-switching is suppressed in the inclined jet, aligning with 2D-PIV measurements from New (2009) for the major-plane inclined-A elliptical jet. Additionally, Figure 13 presents the velocity profiles at $Z/D_e = 0$ for eight moments within a complete cycle. The results indicate that the jet core deviates from the axial direction, leading to a noticeable contraction downstream. This downstream deviation introduces stronger disturbances, increasing flow instability and resulting in more complex deformation and evolution of the merged vortex ring.

In the velocity field of the minor-plane inclined-B elliptical jet, the energy percentages of the first and second pairs of associated modes are 7.70% and 7.56%, respectively, as shown in Fig. 10(c-i). These values are higher than those of the major-plane inclined-A elliptical jet.

Figures 10(c-i, ii) present the PSDs of the time coefficients for the first two mode pairs, revealing that the dominant frequency of the leading Kelvin–Helmholtz (K–H) vortex ring VR1, corresponding to mode pair (1,2), is St = 0.28, while the trailing VR2 in mode pair (3,4) has a frequency of St = 0.61. The difference in frequencies between VR1 and VR2 suggests that many K–H ring-like structures are rarely involved in merging or pairing. Instead, these large-scale vortex rings undergo axis-switching and eventually break down individually. Figures 14(a, b) illustrates the spatial structures of these two mode pairs, along with the instantaneous spatial structures of the flow field at two-time instances for the minor-plane inclined-B nozzle, using the Q-criterion with $Q = 10\ U_0^2/D^2$. The spatial structures of the mode pair (3,4) exhibit a higher frequency compared to the mode pair (1,2). Figures 14(c, d) shows the instantaneous fields at two moments, and their reconstructed flow fields after SPOD are shown in Figs. 15(e) and 15(f), these fields capture the pairing and merging process of VR1 (mode pair (1, 2)) and VR2 (mode pair (3, 4)), as well as a distinct VR3 corresponding to mode pair (3, 4), which does not participate in the merger, corresponding to the different frequencies of the two mode pairs. It is worth noting that the PSDs of velocity in Fig.10(c) do not exhibit the high frequency at St = 0.61, whereas the td-SPOD method effectively extracts large-scale structures at different frequencies and captures these frequency components. Figure 15 visualizes the vortex dynamics of the large-scale ring-like vortex structures in the minor-plane inclined-B jet, showing eight-time instances within a complete cycle of VR1 and VR2. During the merging process, the vortex rings in the inclined-B elliptical jet begin merging at approximately [$X/D_e \approx \pm 0.65$, $Y/D_e \approx 2.2$, $Z/D_e \approx -0.1$] and complete merging at [$X/D_e \approx \pm 0.5$, $Y/D_e \approx 3.1$, $Z/D_e \approx 0.1$]. As seen in Fig. 15(f), the trailing VR2 transitions into a vortex tube at the end of the leading VR1, eventually forming a streamwise vortex structure. Additionally, the axis-switching phenomenon remains present in the minor-plane inclined-B elliptical jet. Figures 15(f-ii, g-ii, h-ii) illustrate that the first axis-switching occurs at $Y/D_e \approx 2.5$, which is consistent with the non-inclined elliptical jet. The velocity distributions in the $Z/D_e = 0$ plane indicate that the vortex ring is skewed toward the lower end of the inclined exit, leading to a more complex merging point and axis-switching process. Once axis-switching is completed, the vortex rings exchange positions between the major and minor axes, eventually inclining in the direction of the minor axis. Following the merged vortex rings, two large-scale vortex rings (VR-3 and VR-4) remain unmerged. Figure

16 presents the evolution of these unmerged vortex rings, reconstructed using mode pairs (1,2) and (3,4), from $t/T = 0.4375$, for the AR = 2, 30° minor-plane inclined-B elliptical jet, with coloring representing the local axial velocity. These vortex rings may have originated from mode (3,4) at the higher frequency of St = 0.61 and, instead of merging downstream, developed and broke down separately. This process does not occur strictly periodically but appears intermittently. The velocity profiles at $X/D_e = 0$ in Fig. 16 reveal that the jet core is deflected away from the axial direction, with the deflection occurring in the $+Z$ direction, which aligns with the mean velocity field cross-section in Fig. 7. Additionally, the merged vortex ring undergoes more complex deformation and evolution further downstream, as observed in the velocity slices.

The pairing and merging of vortex rings are common in elliptical jets and their variants, while they are not strictly repetitive or even periodic, and sometimes individual vortex rings stretch and disintegrate and do not participate in the merger. Besides, for the 30° minor-plane inclined-B elliptical jet, some continuous independent vortex rings will appear. Figure 17 summarizes the vortex ring merger statistics and topology of different types of elliptical jets. In non-inclined elliptical jets, the merger always occurs in the major plane because the vortex portions of the leading vortex ring VR1 and the trailing VR2 in the major-axis direction are both moving closer to the center axis of the jet under the action of self- and mutual induction (Husain and Hussain 1991). While Fig. 17(b) shows that the most merging point in the major-plane inclined-A jet is near the region of the end of the major-plane of the vortex ring, close to the $-X$ direction (the higher end), the location of the merging point by is starting at [$X/D_e \approx -0.5$, $Y/D_e \approx 2.0$, $Z/D_e \approx \pm 0.3$], and end at the [$X/D_e \approx -0.45$, $Y/D_e \approx 2.5$, $Z/D_e \approx \pm 0.35$], the axis-switching is suppressed in the inclined-A jet, the merger occurs before the completion of the axis-switching, and the merger point mainly exists near one end. As shown in Fig. 17(f), the merger of two vortex rings in the inclined-B elliptical jet is conducted during the process of axis-switching, and the coordinate of the merger point is at [$X/D_e \approx \pm 0.65$, $Y/D_e \approx 2.2$, $Z/D_e \approx -0.1$], and end at the [$X/D_e \approx \pm 0.5$, $Y/D_e \approx 3.1$, $Z/D_e \approx 0.1$].

3.4 Mass Entrainment Characteristics

The 3D LPT method represented by the STB algorithm (Schanz, et al. 2016) can be commonly used for tracking the long trajectories of particles to study particle dispersion, mixing, and other transport-related quantities, which can represent the entrainment rate in the flow. While the number of long trajectories of particles in this experimental measurement is small and distributed non-uniformly due to the greater calibration errors in Fig. 3(b-i, ii). Therefore, the mass entrainment characteristics are still evaluated based on the Eulerian velocity field with the spatial derivative dJ/dY of the volume flux $J(Y)$, calculated by (Crow and Champagne 1971, Wygnanski and Fiedler 1970):

$$\frac{d(J/J_0)}{d(Y/D_e)} = \frac{D_e}{J_0}\int_0^{2\pi} rU_r d\theta, \tag{8}$$

the dJ/dY is the integral of the radial velocity on a circle of radius r centered on the jet, and the J_0 is the initial volume flux leaving the non-inclined elliptical nozzle with velocity U_0; J is the volumetric flux at the streamwise position Y from the nozzle exit; r is defined as the radial coordinate, $r = \sqrt{x^2+z^2}$, by interpolating to the cylindrical mesh (Y, r, θ) in each direction from the Cartesian coordinate system (X, Y, Z) defined in the reconstructed volume of Fig. 1, and U_r is the radial velocity. The spatial derivative of the volume flux dJ/dY has been also widely applied to study the mass entrainment of the non-circular jet (El Hassan and Meslem 2010, El Hassan et al. 2011, Meslem et al. 2011, Nastase et al. 2008, Zeng, et al. 2023).

Figure 18 tracks the instantaneous mass entrainment rate variations for elliptical and inclined elliptical jets at $Y/D_e = 2.5$, $r/D_e = 1.25$. The elliptical jet with AR = 2 exhibits superior entrainment characteristics at $Y/D_e = 2.5$ primarily due to axis-switching, as reported in previous work (Zeng, et al. 2023). Therefore, the entrainment rates at this plane are used for comparison. The results show that the mean entrainment rate for the inclined elliptical jets is approximately 11.11% higher for the major-plane inclined-A jet and 27.78% higher for the minor-plane inclined-B jet compared to the non-inclined elliptical jet. Notably, the mean entrainment rate of the non-inclined elliptical jet at AR = 2 is 0.054, which is slightly lower than the 0.055 reported

in (Zeng, et al. 2023). This discrepancy is likely due to measurement uncertainties in the instantaneous flow field. Additionally, larger negative peaks observed between 1.0s and 1.4s result from the strong expansion of a vortex ring as it approaches this plane, causing the fluid in the jet core to enter a negative entrainment state. It is noteworthy that the dominant frequency of this vortex ring corresponds to St = 0.39, aligning with modes (1,2) in the flow field. Unlike conventional vortex structures that undergo pairing and merging, this vortex ring propagates independently through axial switching and movement. The analysis further indicates that better mass entrainment occurs when vortex rings undergo pairing and merging, whereas an isolated large-scale vortex ring can induce significant negative entrainment effects as it traverses a given plane. These findings highlight the complex interactions governing mass entrainment in elliptical jet flows.

The temporal evolution of the entrainment rate has been matched with the instantaneous velocity fields obtained using the Tomo-PIV technique, revealing a clear periodicity. The PSD calculations (performed using a window shift of 512 time-series data per window with an 80% overlap rate) confirm that the periodicity of the mass entrainment rate is strongly correlated with the frequency of large-scale structures across all three jet flows. Our analysis of the relationship between large-scale structures and mass entrainment for the first two mode pairs in these flows shows that the entrainment rate peaks between successive large-scale vortex rings. As shown in Fig. 19(b, e), for the non-inclined elliptical jet, when a K–H vortex ring is about to pass through or is actively traversing the axis-switching plane, the entrainment rate becomes negative, indicating significant flow expansion. From Fig. 19(c), it is evident that after the large-scale K–H vortex ring passes, ambient fluid is entrained into the jet core, leading to an entrainment rate peak. Simultaneously, the trailing vortex ring generates streamwise vortex structures during the merging process in the braid region, drawing a substantial volume of fluid into the jet core (Zeng, et al. 2023). Compared to the non-inclined elliptical jet, a stronger correlation between the vortex ring and entrainment rate is observed in the major-plane inclined-A elliptical jet (Figure 20). This is primarily due to the larger size of the inclined vortex ring, which facilitates the formation of more streamwise vortex structures during the merging of two vortex rings, as illustrated in Fig. 20(d, e). These streamwise vortices are likely the

dominant factor behind the enhanced mass entrainment in this configuration. Similarly, from Figs. 21(b, e), during the merging process of the two vortex rings in the minor-plane inclined-B jet, a substantial number of streamwise structures are generated, significantly enhancing mass entrainment performance. The entrainment enhancement by streamwise structures was also confirmed in the literatures (El Hassan and Meslem 2010, El Hassan, et al. 2011, Meslem, et al. 2011). These findings suggest that adjusting the nozzle outlet geometry can promote the formation of streamwise vortex structures during the evolution of large-scale vortex structures, thereby enhancing mass entrainment efficiency.

4. Conclusion

The dynamic evolution of vortex interactions and their positive effects on entrainment in inclined elliptical jet flows (with inclination angles of 30° in both the major and minor planes) at a Reynolds number of approximately 3,000 are characterized and compared with those of a non-inclined elliptical jet through experimental measurements. These analyses are conducted using time-resolved Tomo-PIV and 3D LPT techniques. To enhance the accuracy of the Eulerian velocity fields obtained from Tomo-PIV, sparse high-precision particle tracks from 3D LPT measurements are incorporated. By integrating these sparse tracks and imposing a zero-divergence constraint on the velocity field, a more accurate velocity reconstruction is achieved. Through sparse track-enhanced volumetric reconstruction, combining Tomo-PIV (2.05 minutes) and 3D LPT (1.67 minutes), an accurate 3D flow field with a grid resolution of $36 \times 70 \times 36$ can be obtained within 2.59 minutes (2.05 + 0.54 minutes), as Tomo-PIV and 3D LPT can be conducted concurrently. The sparse track-enhanced volumetric reconstruction strategy provides an efficient approach for obtaining high-accuracy vector field reconstructions. This method is particularly valuable for real-world 3D experiments and complex engineering applications, where achieving high precision in velocity field measurements is often challenging due to experimental limitations.

The measurement results exhibit reasonable statistical characteristics and indicate that inclined elliptical jets achieve higher entrainment rates than their non-inclined counterparts.

The PSDs and td-SPOD results reveal that the elliptical nozzle at AR = 2 and Re = 3,000 features two dominant frequencies: St = 0.39 and St = 0.28, corresponding to the leading and trailing vortex rings, respectively. For the major-plane inclined-A nozzle, the dominant frequencies of the leading and trailing vortex ring are all at St = 0.28, which shows that the pairing and merging of vortex rings in major-plane 30° inclined-A jet may be a periodic process. After the merging of vortex rings at the position of [$X/D_e \approx$ -0.45, $Y/D_e \approx$ 2.5, $Z/D_e \approx \pm$0.35], the first axis-switching is completed in the major-plane inclined-A elliptical jet at the flow position $Y/D_e \approx$ 3.5, whereas it can be completed in the uninclined elliptical jet at $Y/D_e \approx$ 2.5, which indicates that the axial switching is suppressed in the major-plane inclined-A elliptical jet. Whereas in the minor-plane inclined-B jet flow, the dominant frequencies of the leading and trailing vortex ring are St = 0.28 and St = 0.61, respectively. The merger of two vortex rings in the inclined-B elliptical jet is completed during the process of axis-switching, and the coordinate of the merger point starts at [$X/D_e \approx \pm$0.65, $Y/D_e \approx$ 2.2, $Z/D_e \approx$ -0.1], and end at the [$X/D_e \approx \pm$0.5, $Y/D_e \approx$ 3.1, $Z/D_e \approx$ 0.1]. Sometimes a pair of large-scale vortex rings did not merge downstream, they often developed and broke down separately.

At the axis-switching plane of Y/D_e = 2.5, the mean entrainment rate obtained with inclined elliptical jets is approximately 11.11% (major-plane inclined-A) and 27.78% (minor-plane inclined-B) higher than that obtained with the non-inclined elliptical jet. During the merging process and axis-switching process of the two vortex rings in the two inclined nozzles, a large number of streamwise structures can be generated from the trailing vortex ring, which greatly causes the higher mean entrainment rate. Adjustment of nozzle outlet geometry can make the generation of streamwise vortex structures during large-scale vortex structure movement, enhancing mass entrainment and transport.

Acknowledgments

The authors thank the financial support from the National Natural Science Foundation of China (12272231, 12227803).

Ethics Declarations

This is submitted for publication consideration to *Experiments in Fluids*. The manuscript has been neither published nor submitted elsewhere for publication. If accepted by Experiments in Fluids, it will not be published elsewhere in the same form, in English or in any other language, without the written consent of the publisher.

Competing interests

The authors declare that they have no known competing financial interests or personal relationships that could have appeared to influence the work reported in this paper.

Authors' contributions

Xin ZENG and Hao QU did this experiment and analyzed experimental data, Xin ZENG wrote the main manuscript text and plotted all figures. Chuangxin HE guided the methods of experimental measurement and data analysis, and revised the paper. Yingzheng LIU provided the overall idea of the paper and experiment. Lian GAN provided the CPU Tomo-PIV code(s). All authors reviewed the manuscript.

Funding

This work was supported by the National Natural Science Foundation of China (12272231, 12227803).

Availability of data and materials

The data that support the findings of this study are available upon reasonable request from the authors.

References

Atkinson C, Coudert S, Foucaut J-M, Stanislas M, Soria J (2011) The accuracy of tomographic particle image velocimetry for measurements of a turbulent boundary layer. Experiments in Fluids 50:1031-1056. https://doi.org/10.1007/s00348-010-1004-z

Bardet PM, Peterson PF, Savaş Ö (2010) Split-screen single-camera stereoscopic PIV application to a turbulent confined swirling layer with free surface. Experiments in Fluids 49:513-524. https://doi.org/10.1007/s00348-010-0823-2

Behrouzi P, McGuirk JJ, Avenell C (2017) Effect of Scarfing on Rectangular Nozzle Supersonic Jet Plume Flow Characteristics. Aiaa Journal 56:301-315. https://doi.org/10.2514/1.J055526

Bhapkar US, Srivastava A, Agrawal A (2014) Acoustic and heat transfer characteristics of an impinging elliptical synthetic jet generated by acoustic actuator. International Journal of Heat and Mass Transfer 79:12-23. https://doi.org/10.1016/j.ijheatmasstransfer.2014.07.083

Cater JE, Soria J (2002) The evolution of round zero-net-mass-flux jets. Journal of Fluid Mechanics 472:167-200. https://doi.org/10.1017/S0022112002002264

Crow SC, Champagne FH (1971) Orderly structure in jet turbulence. Journal of Fluid Mechanics 48:547-591. https://doi.org/10.1017/S0022112071001745

Das R, Girimaji SS (2022) The effect of large-scale forcing on small-scale dynamics of incompressible turbulence. Journal of Fluid Mechanics 941:A34. https://doi.org/10.1017/jfm.2022.288

El Hassan M, Meslem A (2010) Time-resolved stereoscopic particle image velocimetry investigation of the entrainment in the near field of circular and daisy-shaped orifice jets. Physics of Fluids 22:035107. https://doi.org/10.1063/1.3358465

El Hassan M, Meslem A, Abed-Meraim K (2011) Experimental investigation of the flow in the near-field of a cross-shaped orifice jet. Physics of Fluids 23:045101. https://doi.org/10.1063/1.3562841

Elsinga GE, Scarano F, Wieneke B, Oudheusden BWV (2006) Tomographic particle image velocimetry. Experiments in Fluids 41:933-947. https://doi.org/10.1007/s00348-006-0212-z

Gan L, Cardesa-Duenas JI, Michaelis D, Dawson J (2012) Comparison of Tomographic PIV algorithms on resolving coherent structures in locally isotropic turbulence. 16th International Symposium on Applications of Laser Techniques to Fluid Mechanics Lisbon, Portugal, pp 9-12

Gesemann S (2018) Optimizations of optical flow measurement systems. Dissertation, Georg-August-Universität Göttingen.

Gesemann S, Huhn F, Schanz D, Schröder A (2016) From noisy particle tracks to velocity, acceleration and pressure fields using B-splines and penalties. 18th International Symposium on the Application of Laser and Imaging Techniques to Fluid Mechanics Lisboa, Portugal, pp 4-7

He C, Liu Y, Gan L (2021) Dynamics of the jet flow issued from a lobed Nozzle: Tomographic particle image velocimetry measurements. International Journal of Heat and Fluid Flow 89:108795. https://doi.org/10.1016/j.ijheatfluidflow.2021.108795

He C, Wang P, Liu Y, Gan L (2022) Flow enhancement of tomographic particle image velocimetry measurements using sequential data assimilation. Physics of Fluids 34:035101. https://doi.org/10.1063/5.0082460

He X, Lustbader JA, Arik M, Sharma R (2015) Heat transfer characteristics of impinging steady and synthetic jets over vertical flat surface. International Journal of Heat and Mass Transfer 80:825-834. https://doi.org/10.1016/j.ijheatmasstransfer.2014.08.006

Husain HS, Hussain F (1991) Elliptic jets. Part 2. Dynamics of coherent structures: pairing. Journal of Fluid Mechanics 233:439-482. https://doi.org/10.1017/S0022112091000551

Hussain F, Husain HS (1989) Elliptic jets. Part 1. Characteristics of unexcited and excited jets. Journal of Fluid Mechanics 208:257-320. https://doi.org/10.1017/S0022112089002843

Hussein HJ, Capp SP, George WK (1994) Velocity measurements in a high-Reynolds-number, momentum-conserving, axisymmetric, turbulent jet. Journal of Fluid Mechanics 258:31-75. https://doi.org/10.1017/S002211209400323X

Jeong J, Hussain F (1995) On the identification of a vortex. Journal of Fluid Mechanics 285:69-94. https://doi.org/10.1017/S0022112095000462

Karami S, Soria J (2018) Analysis of coherent structures in an under-expanded supersonic impinging jet using spectral proper orthogonal decomposition (SPOD). Aerospace 5:73. https://doi.org/10.3390/aerospace5030073

Kumar B, Verma SK, Srivastava S (2021) Mixing Characteristics of Supersonic Jet from Bevelled Nozzles. International Journal of Heat and Technology 39:559-572. https://doi.org/10.18280/ijht.390226

Li Y, Perlman E, Wan M, et al. (2008) A public turbulence database cluster and applications to study Lagrangian evolution of velocity increments in turbulence. Journal of Turbulence 9:1-29. https://doi.org/10.1080/14685240802376389

Lim HD, Ding J, Shi S, New TH (2020) Proper orthogonal decomposition analysis of near-field coherent structures associated with V-notched nozzle jets. Experimental Thermal and Fluid Science 112:109972. https://doi.org/https://doi.org/10.1016/j.expthermflusci.2019.109972

Lim HD, New TH, Mariani R, Cui YD (2018) Visual hull based 3D reconstruction of shocks in under-expanded supersonic bevelled jets. Experimental Thermal and Fluid Science 99:458-473. https://doi.org/10.1016/j.expthermflusci.2018.08.022

Lim TT (1998) On the breakdown of vortex rings from inclined nozzles. Physics of Fluids 10:1666-1671. https://doi.org/10.1063/1.869684

Long J, New TH (2016) Vortex dynamics and wall shear stress behaviour associated with an elliptic jet impinging upon a flat plate. Experiments in Fluids 57:121. https://doi.org/10.1007/s00348-016-2206-9

Lumley JL (1967) The structure of inhomogeneous turbulent flows. Atmospheric turbulence and radio wave propagation:166-178. https://doi.org/10.1002/nme.4403

Meslem A, El Hassan M, Nastase I (2011) Analysis of jet entrainment mechanism in the transitional regime by time-resolved PIV. Journal of Visualization 14:41-52. https://doi.org/10.1007/s12650-010-0057-7

Nastase I, Meslem A, Gervais P (2008) Primary and secondary vortical structures contribution in the entrainment of low Reynolds number jet flows. Experiments in Fluids 44:1027-1033. https://doi.org/10.1007/s00348-008-0488-2

New TH (2009) An experimental study on jets issuing from elliptic inclined nozzles. Experiments in Fluids 46:1139-1157. https://doi.org/10.1007/s00348-009-0622-9

New TH, Tsioli E (2014) Effects of area-ratio on the near-field flow characteristics and deflection of circular inclined coaxial jets. Experimental Thermal and Fluid Science 54:225-236. https://doi.org/10.1016/j.expthermflusci.2013.12.022

New TH, Tsovolos D (2011) On the vortical structures and behaviour of inclined elliptic jets. European Journal of Mechanics-B/Fluids 30:437-450. https://doi.org/10.1016/j.euromechflu.2011.04.006

New TH, Tsovolos D (2012) Vortex Behaviour and Velocity Characteristics of Jets Issuing from Hybrid Inclined Elliptic Nozzles. Flow, Turbulence and Combustion 89:601-625. https://doi.org/10.1007/s10494-012-9411-2

New TH, Tsovolos D (2013) On the vortex structures and behaviour of notched elliptic jets. Experimental Thermal and Fluid Science 49:51-66. https://doi.org/https://doi.org/10.1016/j.expthermflusci.2013.03.009

New TH, Tsovolos D, Tsioli E (2015) Dynamics of Jets Issuing from Trailing-Edge Modified Nozzles. In: New DTH and Yu SCM (eds) Vortex Rings and Jets: Recent Developments in Near-Field Dynamics. Springer Singapore, Singapore, pp 145-189. https://doi.org/10.1007/978-981-287-396-5_5

Pereira F, Gharib M (2002) Defocusing digital particle image velocimetry and the three-dimensional characterization of two-phase flows. Measurement Science and Technology 13:683. https://doi.org/10.1088/0957-0233/13/5/305

Pereira F, Gharib M, Dabiri D, Modarress D (2000) Defocusing digital particle image velocimetry: a 3-component 3-dimensional DPIV measurement technique. Application to bubbly flows. Experiments in Fluids 29:S078-S084. https://doi.org/10.1007/s003480070010

Quinn WR (1992) Turbulent free jet flows issuing from sharp-edged rectangular slots: The influence of slot aspect ratio. Experimental Thermal and Fluid Science 5:203-215. https://doi.org/10.1016/0894-1777(92)90007-R

Rao SMV, Karthick SK, Anand A (2020) Elliptic supersonic jet morphology manipulation using sharp-tipped lobes. Physics of Fluids 32:086107. https://doi.org/10.1063/5.0015035

Rowley CW, Mezić I, Bagheri S, Schlatter P, Henningson DS (2009) Spectral analysis of nonlinear flows. Journal of Fluid Mechanics 641:115-127. https://doi.org/10.1146/annurev-fluid-010816-060042

Scarano F, Elsinga GE, Bocci E, van Oudheusden BW (2006) Investigation of 3-D coherent structures in the turbulent cylinder wake using Tomo-PIV. 13th Int Symp on Applications of Laser Techniques to Fluid Mechanics. Lisbon Portugal

Schanz D, Gesemann S, Schrder A (2016) Shake-The-Box: Lagrangian particle tracking at high particle image densities. Experiments in Fluids 57:70. https://doi.org/10.1007/s00348-016-2157-1

Schmid PJ (2010) Dynamic mode decomposition of numerical and experimental data. Journal of Fluid Mechanics 656:5-28. https://doi.org/10.1017/S0022112010001217

Schmidt OT, Towne A, Rigas G, Colonius T, Brès GA (2018) Spectral analysis of jet turbulence. Journal of Fluid Mechanics 855:953-982. https://doi.org/10.1017/jfm.2018.675

Schröder A, Schanz D (2022) 3D Lagrangian particle tracking in fluid mechanics. Annual Review of Fluid Mechanics 55:511-540. https://doi.org/10.1146/annurev-fluid-031822-041721

Shi S, New TH (2013) Some observations in the vortex-turning behaviour of noncircular inclined jets. Experiments in Fluids 54:1614. https://doi.org/10.1007/s00348-013-1614-3

Shi X-D, Feng L-H, Wang J-J (2019) Evolution of elliptic synthetic jets at low Reynolds number. Journal of Fluid Mechanics 868:66-96. https://doi.org/10.1017/jfm.2019.162

Sieber M, Paschereit CO, Oberleithner K (2016) Spectral proper orthogonal decomposition. Journal of Fluid Mechanics 792:798-828. https://doi.org/10.1017/jfm.2016.103

Sirovich L (1987) Turbulence and the dynamics of coherent structures. II. Symmetries and transformations. Quarterly of Applied mathematics 45:573-582. https://doi.org/10.1090/qam/910463

Tan S, Salibindla A, Masuk AUM, Ni R (2020) Introducing OpenLPT: new method of removing ghost particles and high-concentration particle shadow tracking. Experiments in Fluids 61:1-16.

Towne A, Schmidt OT, Colonius T (2018) Spectral proper orthogonal decomposition and its relationship to dynamic mode decomposition and resolvent analysis. Journal of Fluid Mechanics 847:821-867. https://doi.org/10.1017/jfm.2018.283

Troolin DR, Longmire EK (2010) Volumetric velocity measurements of vortex rings from inclined exits. Experiments in Fluids 48:409-420. https://doi.org/10.1007/s00348-009-0745-z

Vieillefosse P (1984) Internal motion of a small element of fluid in an inviscid flow. Physica A: Statistical Mechanics and its Applications 125:150-162. https://doi.org/https://doi.org/10.1016/0378-

4371(84)90008-6
Wall ME, Rechtsteiner A, Rocha LM (2003) Singular value decomposition and principal component analysis A practical approach to microarray data analysis. Springer, pp 91-109. https://doi.org/10.1007/0-306-47815-3_5
Webster DR, Longmire EK (1997) Vortex dynamics in jets from inclined nozzles. Physics of Fluids 9:655-666. https://doi.org/10.1063/1.869223
Webster DR, Longmire EK (1998) Vortex rings from cylinders with inclined exits. Physics of Fluids 10:400-416. https://doi.org/10.1063/1.869531
Wieneke B (2008) Volume self-calibration for 3D particle image velocimetry. Experiments in Fluids 45:549-556. https://doi.org/10.1007/s00348-008-0521-5
Wieneke B (2013) Iterative reconstruction of volumetric particle distribution. Measurement Science & Technology 24:827-837. https://doi.org/10.1088/0957-0233/24/2/024008
Wlezien RW, Kibens V (1986) Passive control of jets with indeterminate origins. Aiaa Journal 24:1263-1270. https://doi.org/10.2514/3.9430
Wlezien RW, Kibens V (1988) Influence of nozzle asymmetry on supersonic jets. Aiaa Journal 26:27-33. https://doi.org/10.2514/3.9846
Worth N (2010) Tomographic PIV measurement of coherent dissipation scale structures. Dissertation, University of Cambridge. https://doi.org/https://doi.org/10.17863/CAM.13993
Wu J, Lim HD, Wei X, New TH, Cui YD (2018) Flow Characterization of Supersonic Jets Issuing From Double-Beveled Nozzles. Journal of Fluids Engineering 141. https://doi.org/10.1115/1.4040447
Wygnanski I, Fiedler HE (1970) The two-dimensional mixing region. Journal of Fluid Mechanics 41:327-361. https://doi.org/10.1017/S0022112070000630
Zeng X, He C, Liu Y (2022) GPU-accelerated MART and concurrent cross-correlation for tomographic PIV. Experiments in Fluids 63:1-18. https://doi.org/10.1007/s00348-022-03444-3
Zeng X, Qu H, He C, Liu Y, Gan L (2024) A polynomial model with line-of-sight constraints for Lagrangian particle tracking under interface refraction. Measurement Science and Technology 35:066011. https://doi.org/10.1088/1361-6501/ad34ec
Zeng X, Zhang Y, He C, Liu Y (2023) Dynamics and entrainment mechanism of the jet flows from an elliptical nozzle: time-resolved tomographic PIV measurements. Experiments in Fluids 64:142. https://doi.org/10.1007/s00348-023-03683-y

Figure 1

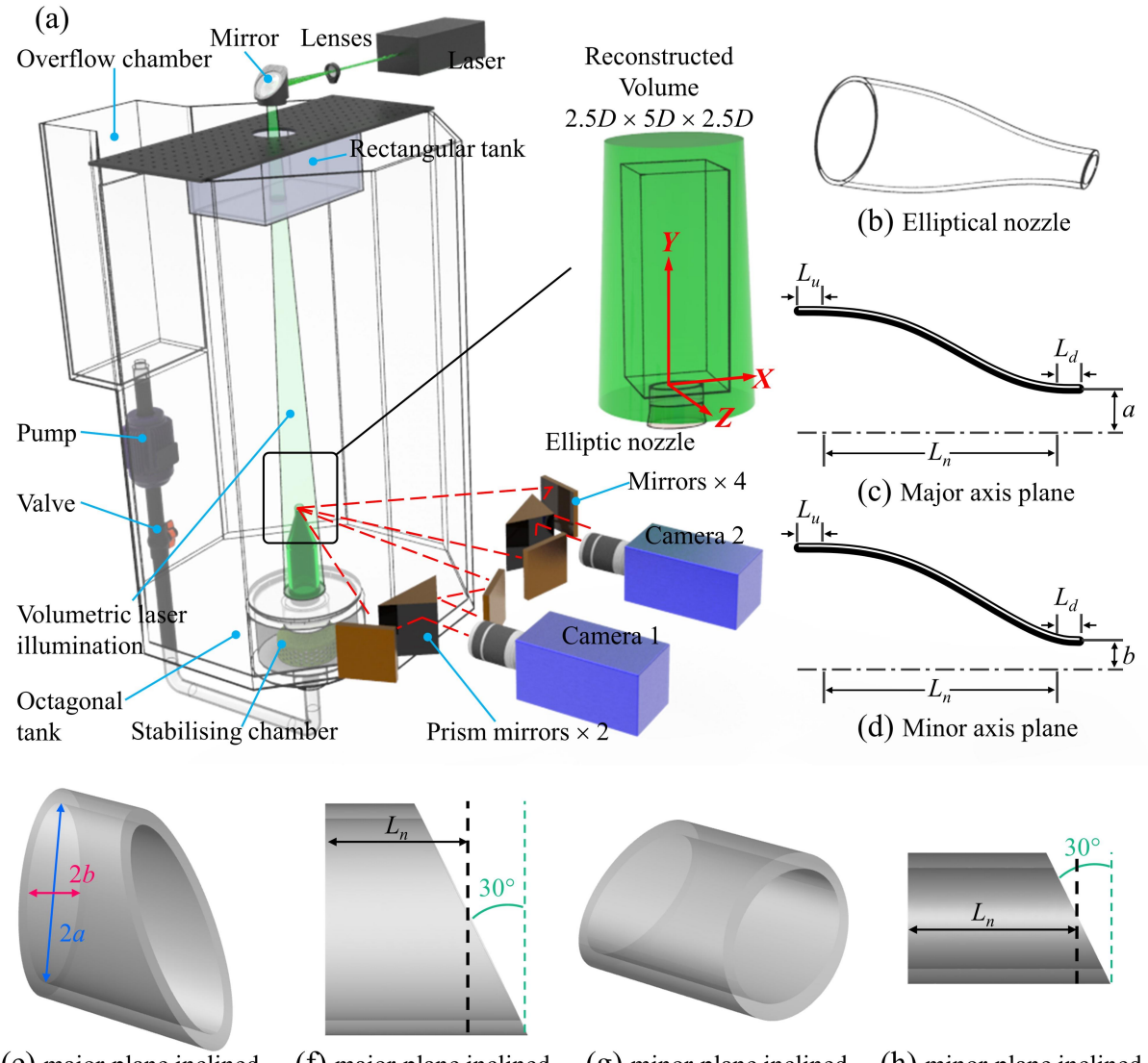

(a) Schematic diagrams of the measurement setup, (b) Elliptic nozzle exit geometry and contour shape in the major-axis plane (c) and the minor-axis plane (d); L_n is the nozzle length, L_u and L_d are lengths of straight portions at the upstream and downstream ends of the nozzle. Designs of the (e)(f) 30° major-plane inclined-A and (g)(h) 30° minor-plane inclined-B elliptic nozzles.

Figure 2

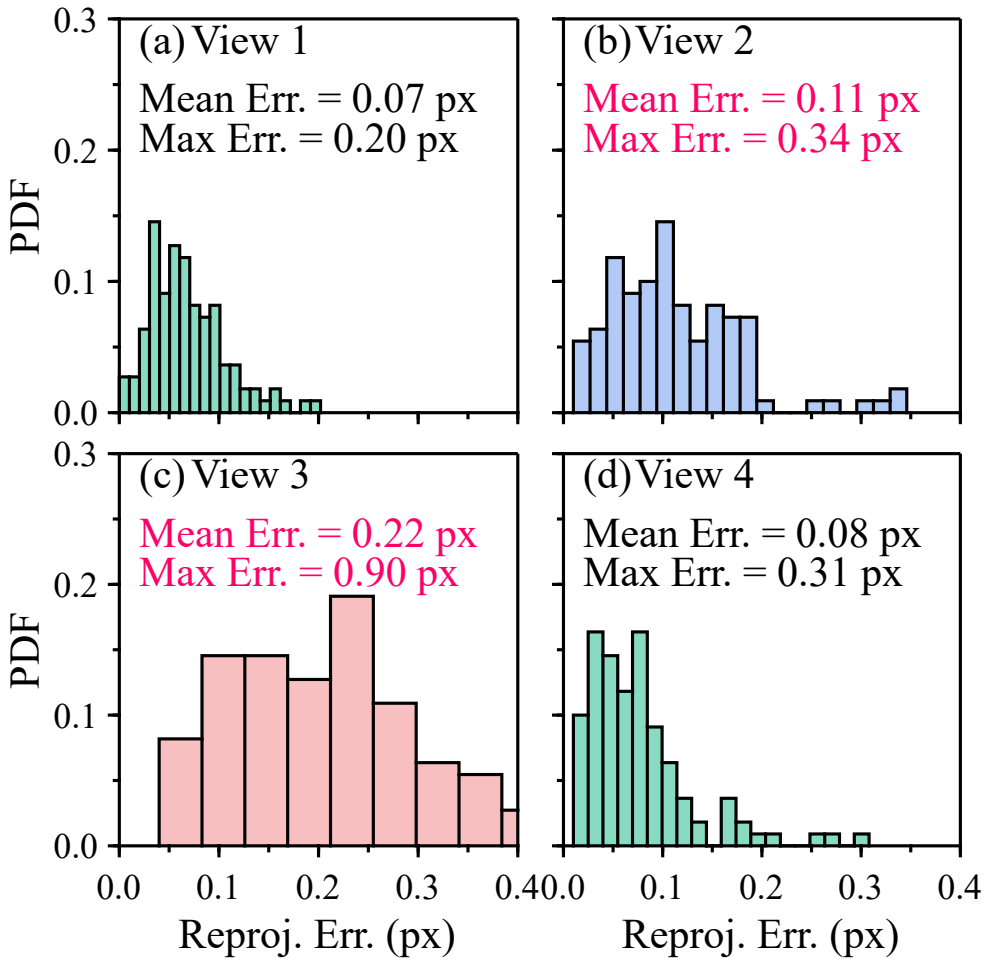

Reprojection errors in inclined elliptical jet experiments with third-order polynomial calibration based on two planes. (a-d) different views

Figure 3

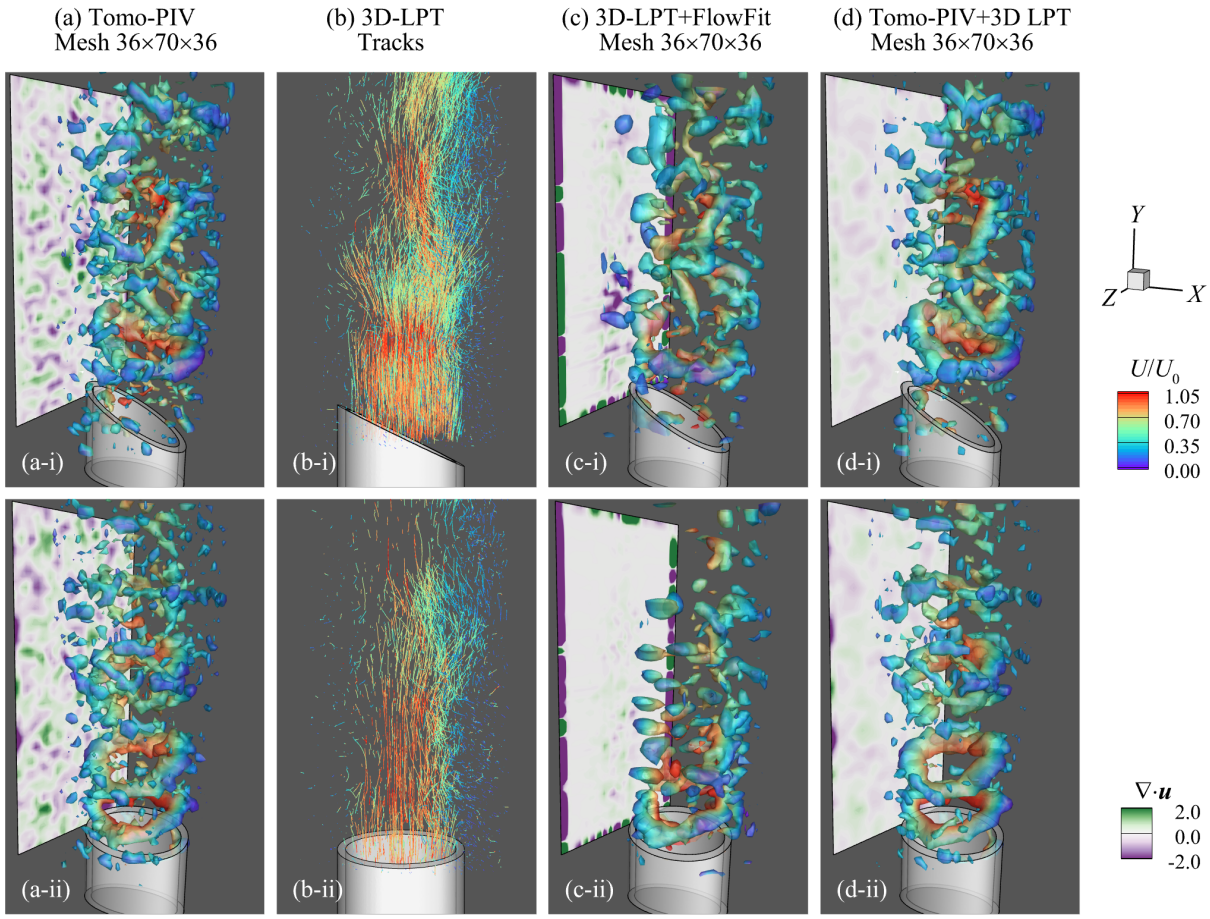

(a-i, ii) Tomo-PIV reconstruction of the velocity field. (b-i, ii) Tracks overlay of 200 time-steps, colored by streamwise velocity. (c-i, ii) Velocity field by FlowFit reconstruction from 3D LPT tracks. (d-i, ii) Velocity field after sparse track-enhanced volumetric reconstruction. (i) and (ii) are 30° major-plane inclined-A and 30° minor-plane inclined-B, respectively. With iso-surfaces of $Q = 0.5\ U_0^2/D_e^2$

Figure 4

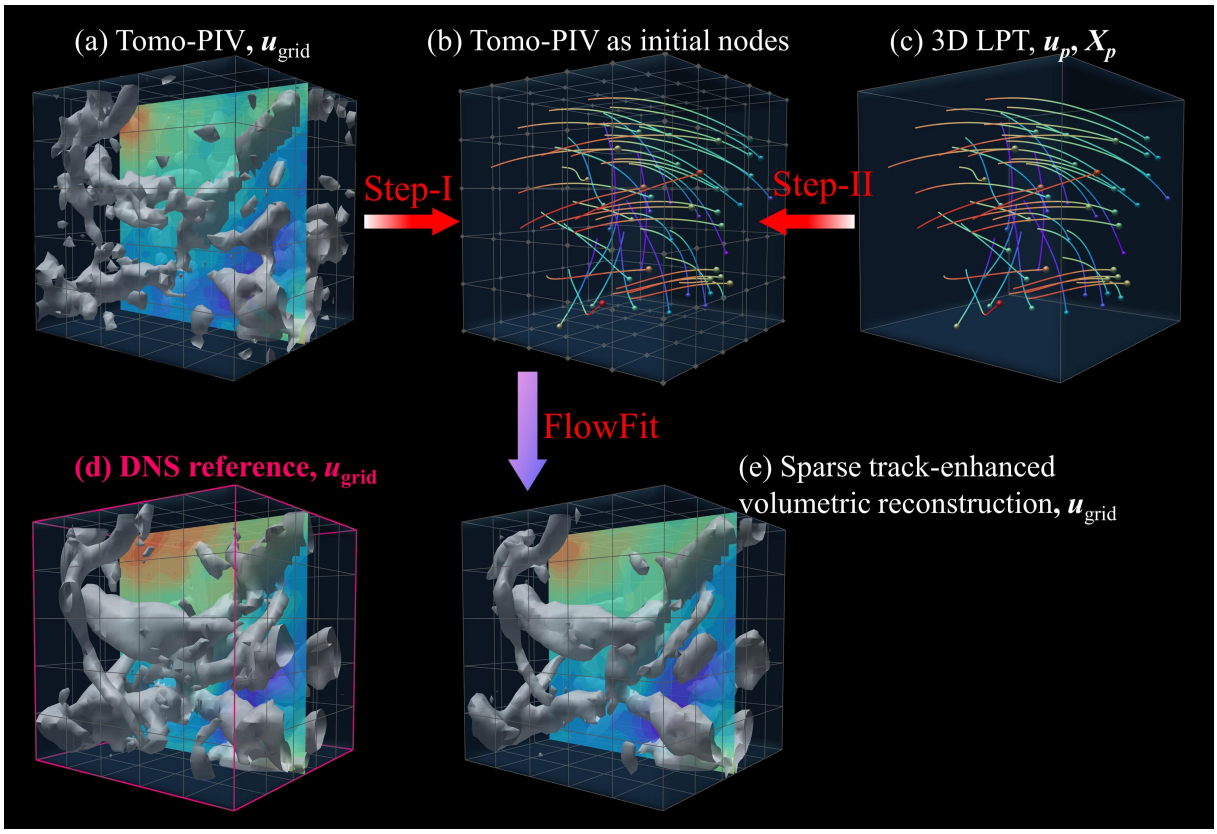

Sparse track-enhanced volumetric reconstruction strategy based on Tomo-PIV and 3D LPT, the schematic diagram is a validation based on the Johns Hopkins DNS Turbulence database (JHTDB) with a grid of 32 × 32 × 32, number of particles is 4,000.

Figure 5

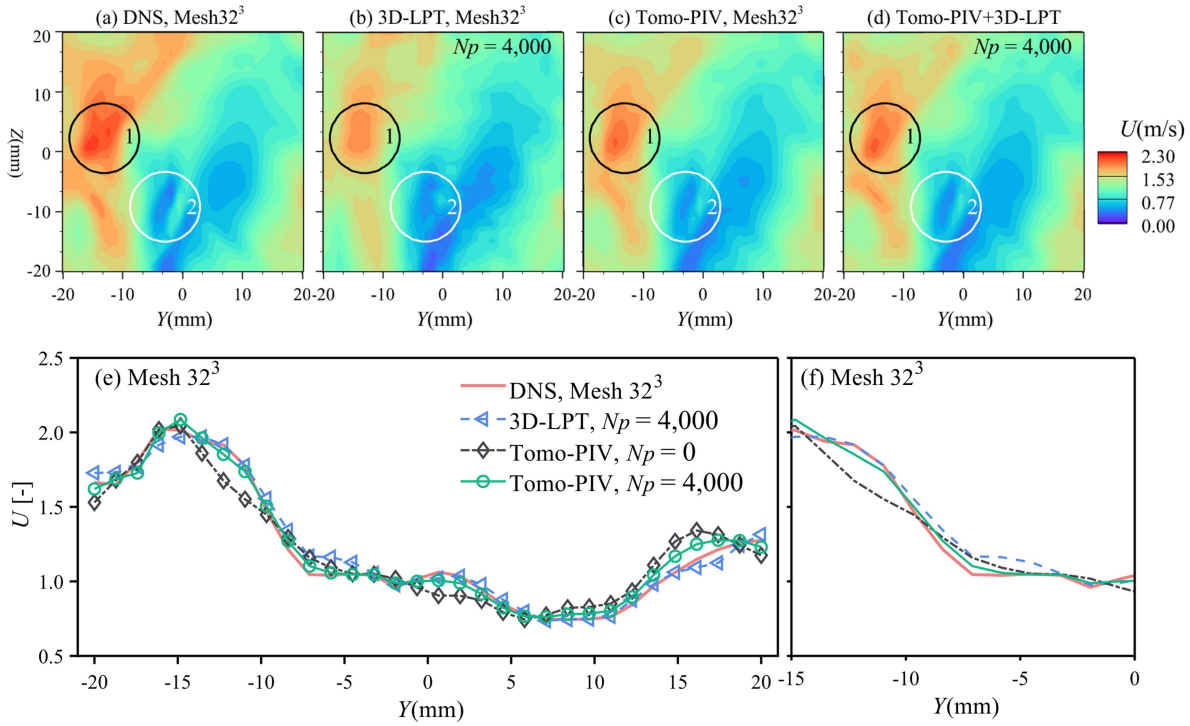

Comparison of velocity distributions at cross section by different velocity reconstruction modes at $X = 0$ mm. (a) DNS reference data, (b) FlowFit from 3D LPT, (c) Flow field by Tomo-PIV, (d) Tomo-PIV+3D LPT. (e) Comparison of velocity field reconstruction accuracy by different velocity reconstruction modes along the Y-axis center line, at $X = 0$ mm, $Z = 0$ mm, $Y \in$ [-20 mm, 20 mm], (f) is local of (e).

Figure 6

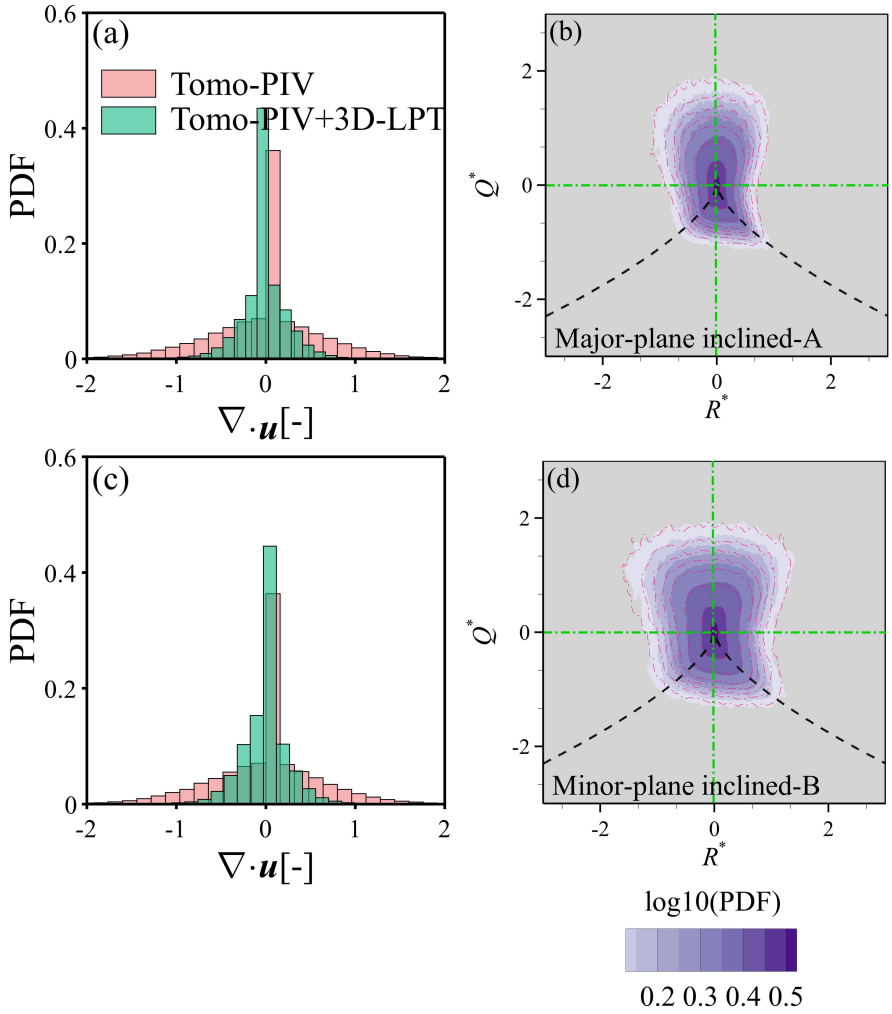

Velocity divergence values and Joint PDFs of the velocity gradient invariables Q^* and R^* for different nozzles before and after sparse track-enhanced volumetric reconstruction. (a) Velocity divergence statistical distribution for 30° major-plane inclined-A nozzle. (b) Joint PDFs of 30° major-plane inclined-A before and after sparse track-enhanced volumetric reconstruction; (c) Velocity divergence statistical distribution for 30° minor-plane inclined-B. (d) Joint PDFs of 30° minor-plane inclined-B before and after sparse track-enhanced volumetric reconstruction.

Figure 7

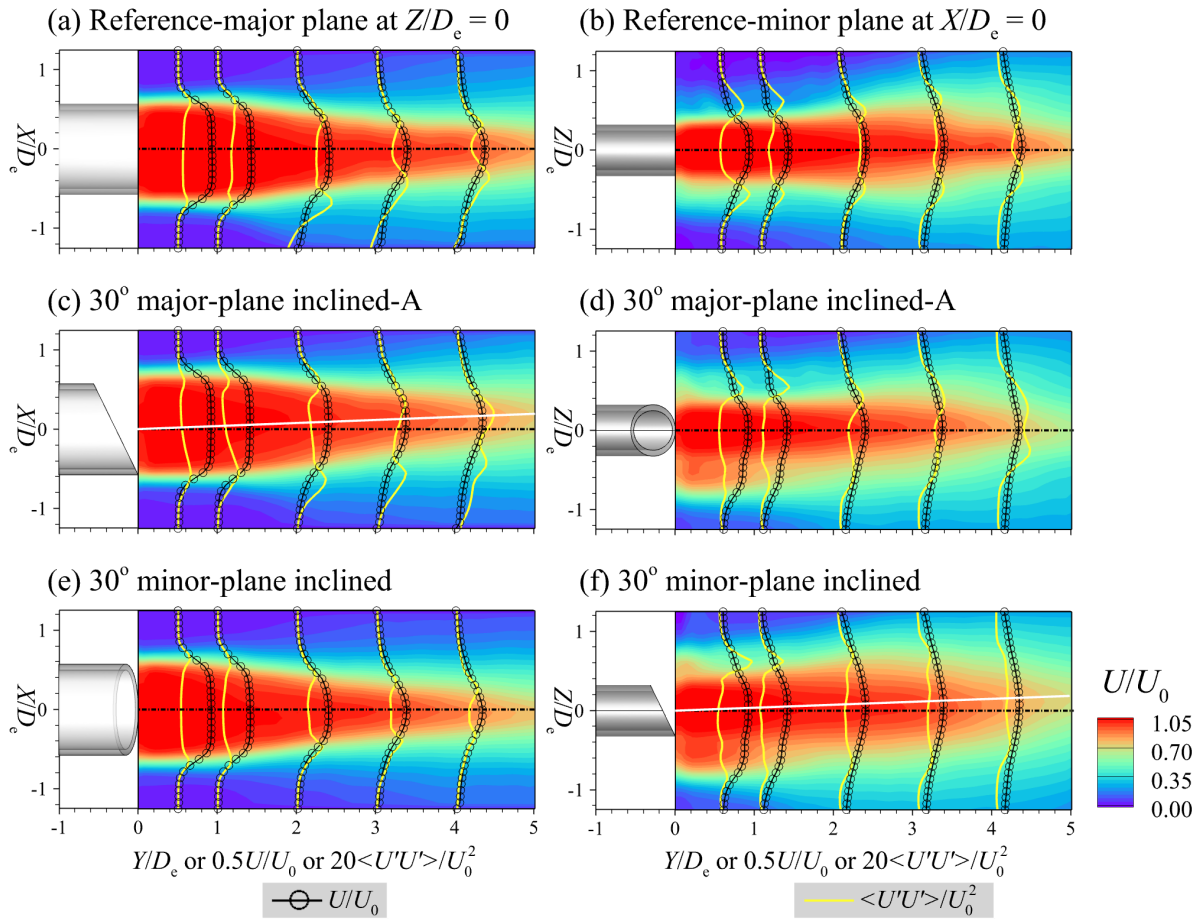

Velocity field and mean fluctuating profiles in major and minor planes of 3D mean velocity field, (a)(b) Reference, AR = 2, (c)(d) 30° major-plane inclined, and (e)(f) 30° minor-plane inclined elliptic nozzles.

Figure 8

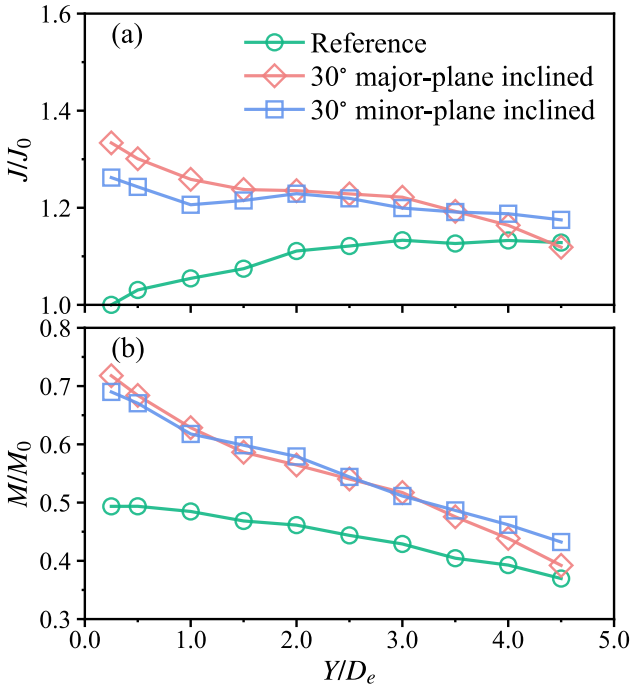

(a) Volume flux J along the streamwise direction, where J_0 is the thrust volume during the blowing period.
(b) Streamwise evolution of the momentum flux

Figure 9

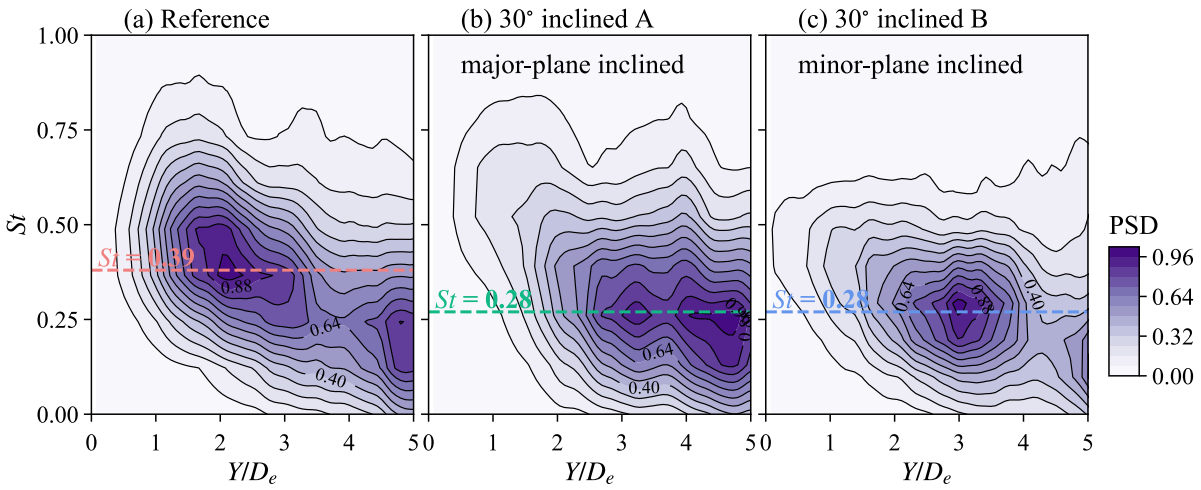

Power spectral density (PSD) [$(m/s)^2$/Hz] of U/U_0 on the centerline of the jet: (a) Reference, AR = 2, (b) 30° major-plane inclined-A, and (c) 30° minor-plane inclined-B elliptic nozzles. Contours of St-PSD are normalized by the maximum value. The contour lines are drawn for 0.40, 0.64, 0.88, and 0.96.

Figure 10

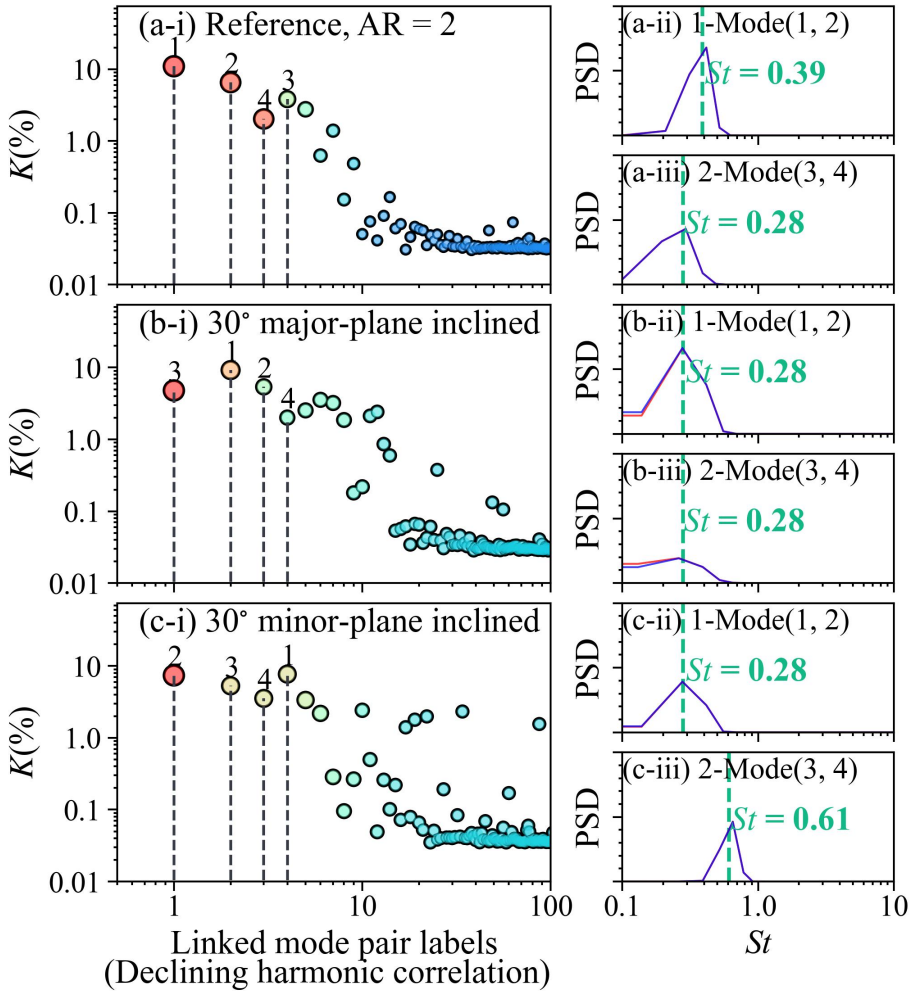

(i) Energy contribution of mode pairs to the dynamics of the flow obtained by td-SPOD, where the circle size and color (red and blue) represent the degree of harmonic correlation (spectral proximity), with larger circles or deeper red shades indicating a stronger correlation. The horizontal labels of "linked mode pair labels" are ordered based on declining harmonic correlation, and the four mode pairs with the highest correlation are then sequentially renumbered 1-4 according to their decreasing energy, note that the most correlated pair of modes (the darkest color) does not necessarily correspond to the highest energy. (ii) and (iii) are PSDs of the temporal coefficients of td-SPOD mode pairs. (a) Reference, AR = 2, (b) 30° major-plane inclined-A, and (c) 30° minor-plane inclined-B elliptic nozzles.

Figure 11

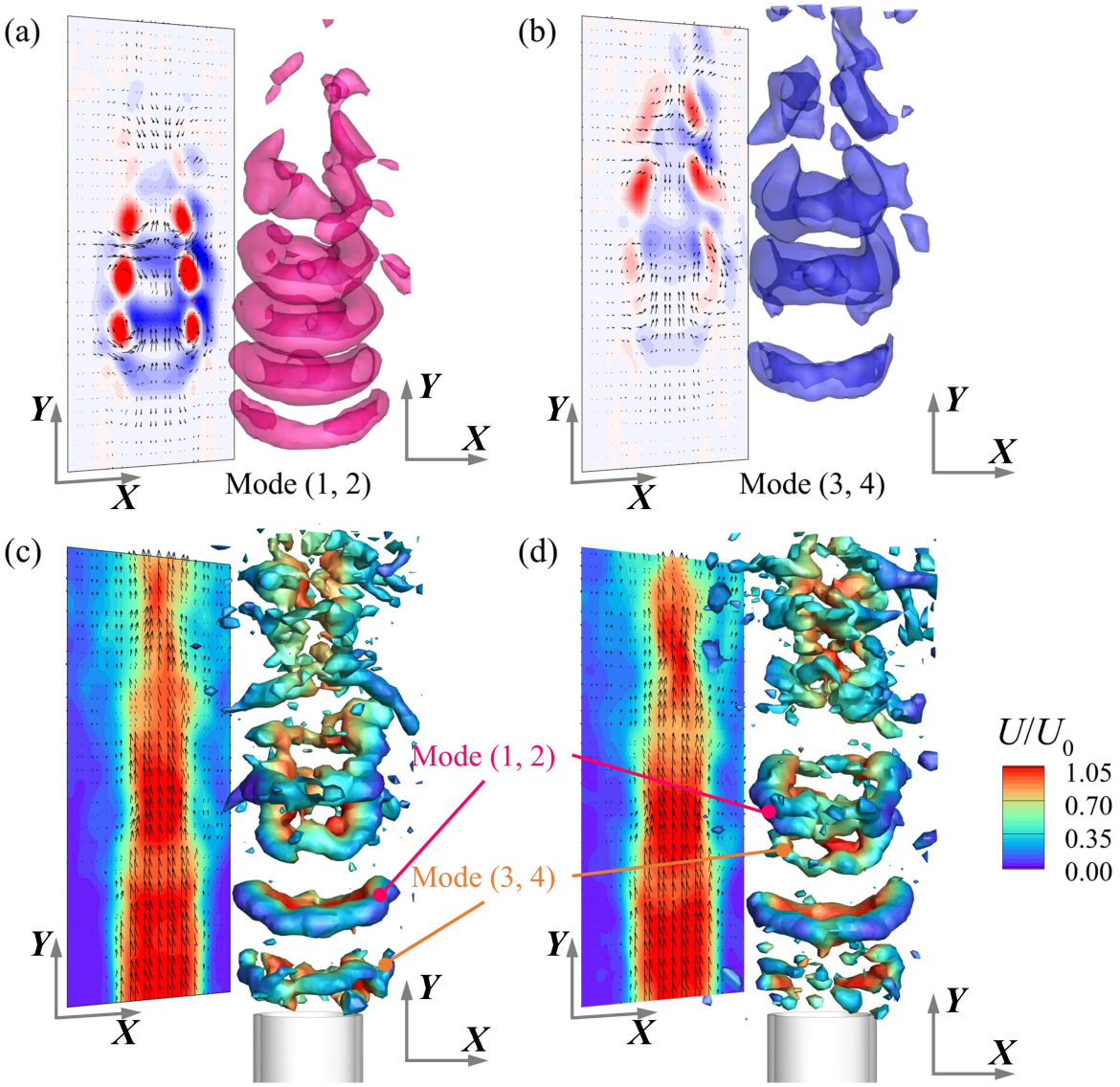

Spatial characteristics of (a) Mode (1, 2) and (b) Mode (3, 4) with iso-surfaces of Q = 10 U_0^2/D^2, the Q criterion for only one of the modes is displayed. And instantaneous velocity field at two moments (c, d) with iso-surfaces of Q = 0.5 U_0^2/D^2 for the elliptical jet at AR = 2, reference, colored by the local axial velocity.

Figure 12

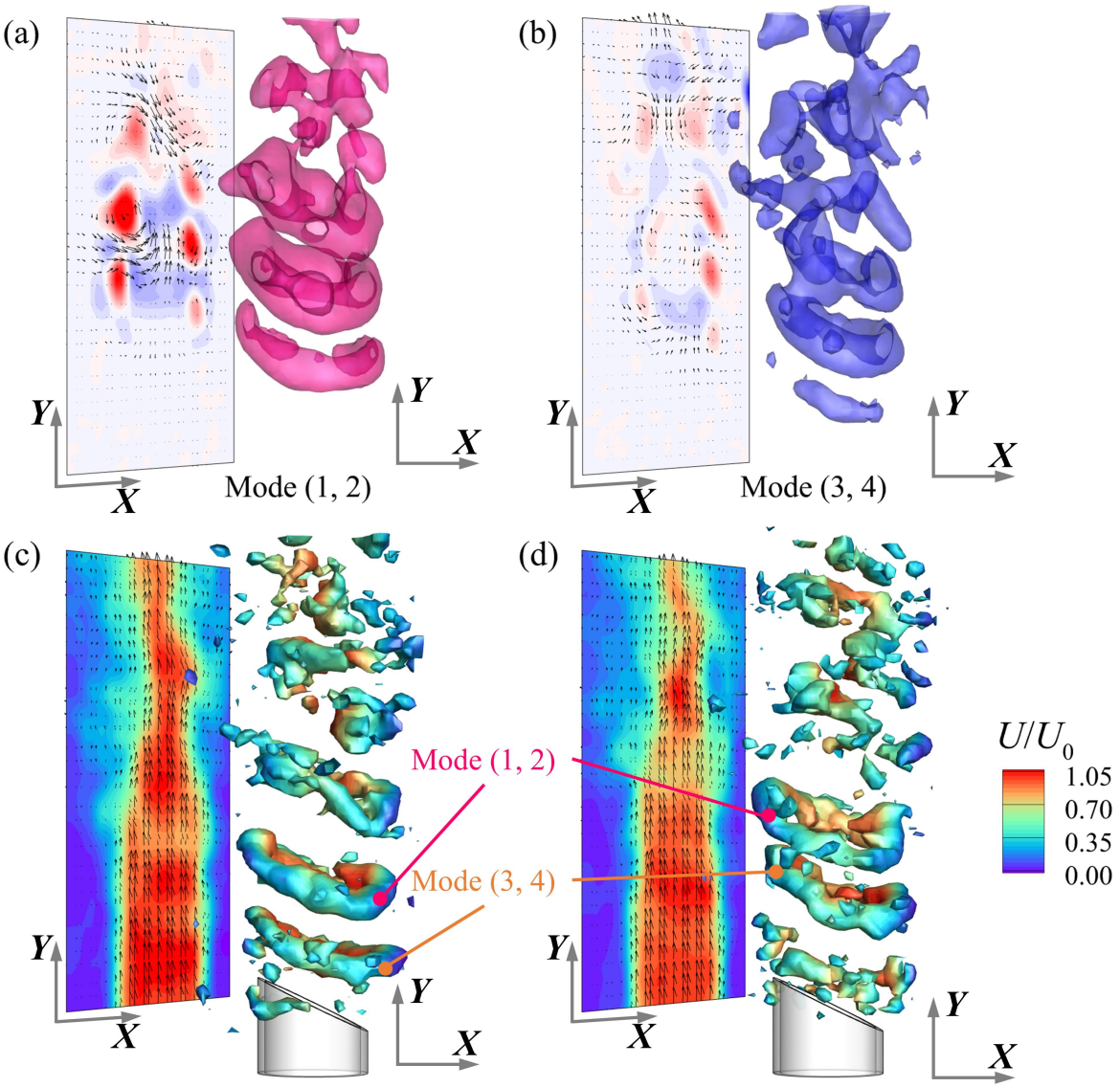

Spatial characteristics of (a) Mode (1, 2) and (b) Mode (3, 4) with iso-surfaces of Q = 10 U_0^2/D^2, the Q criterion for only one of the modes is displayed. And instantaneous velocity field at two moments (c, d) with iso-surfaces of Q = 0.5 U_0^2/D^2 for the major-plane inclined-A elliptical jet, colored by the local axial velocity

Figure 13

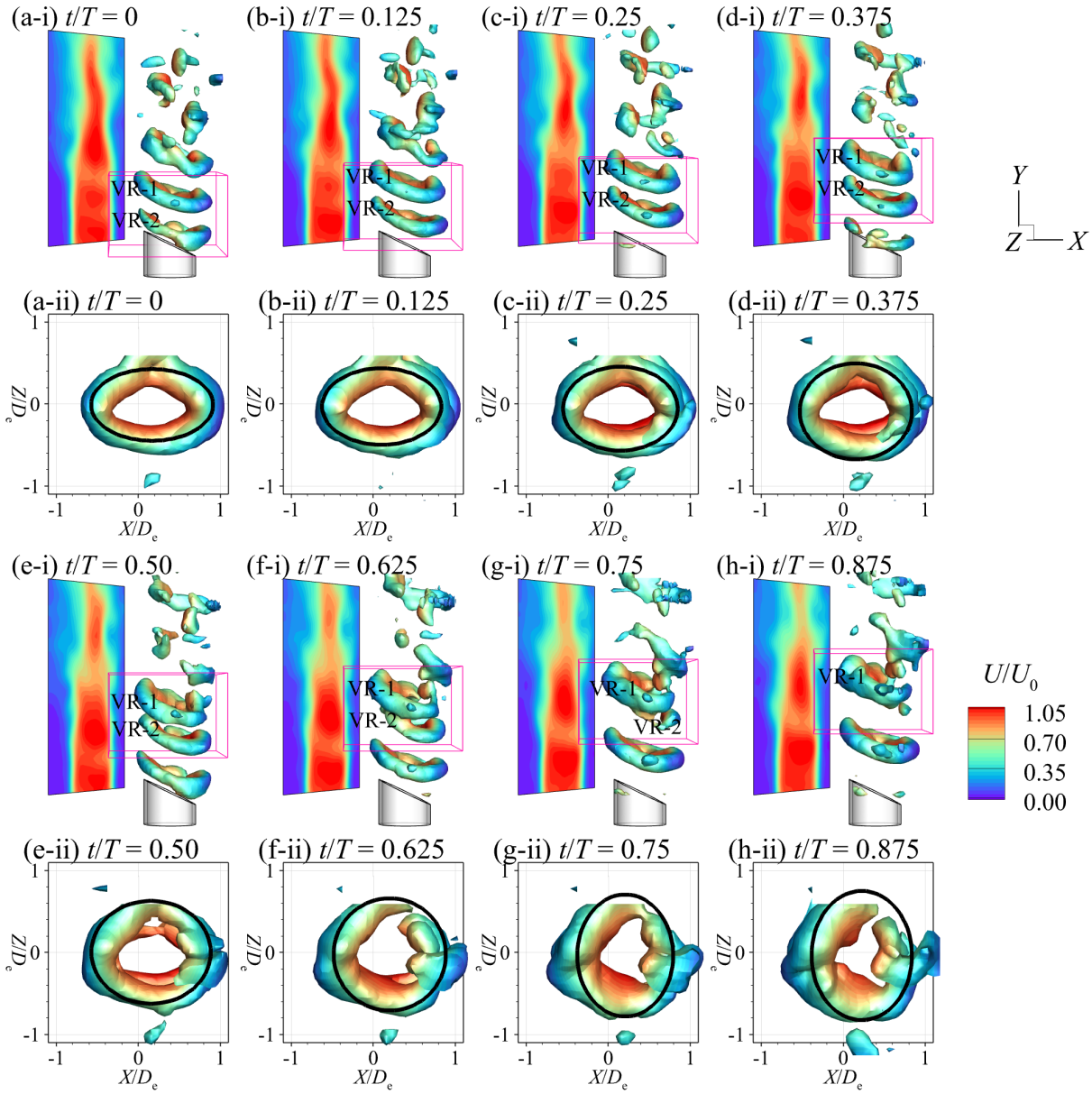

Evolution of vortex rings reconstructed with mode pair (1, 2) and mode pair (3, 4), for the AR = 2, 30° major-plane inclined-A elliptical jet, colored by the local axial velocity. (a) $t/T = 0$. (b) $t/T = 0.125$. (c) $t/T = 0.25$. (d) $t/T = 0.375$. (e) $t/T = 0.50$. (f) $t/T = 0.625$. (g) $t/T = 0.75$. (h) $t/T = 0.875$. (i) presents the 3-D structures, (ii) shows the concerned vortex ring pair structure.

Figure 14

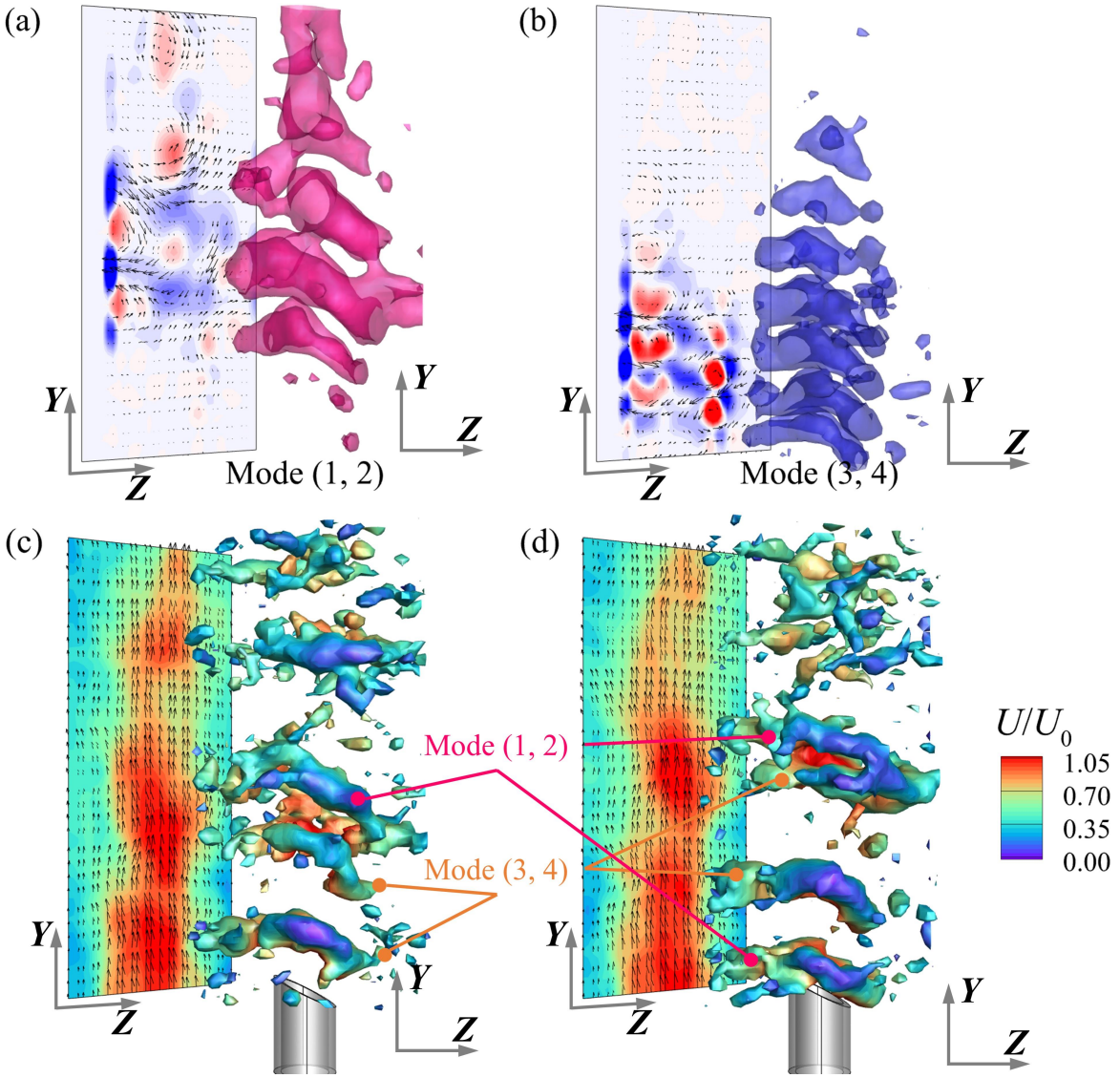

Spatial characteristics of (a) Mode (1, 2) and (b) Mode (3, 4) with iso-surfaces of Q = 10 U_0^2/D^2, the Q criterion for only one of the modes is displayed. And instantaneous velocity field at two moments (c, d) with iso-surfaces of Q = 0.5 U_0^2/D^2 for the minor-plane inclined-B elliptical jet, colored by the local axial velocity

Figure 15

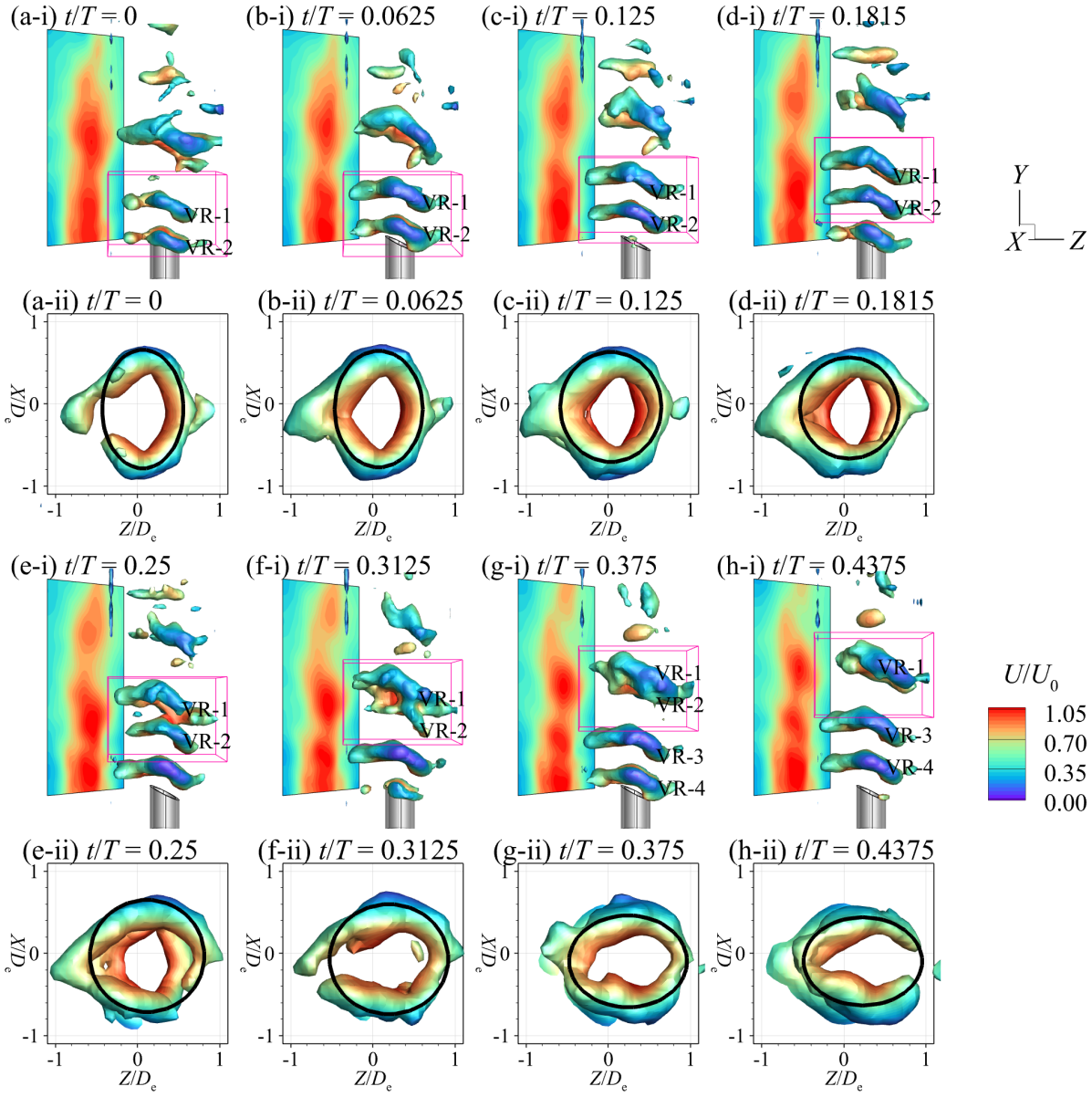

Evolution of vortex rings reconstructed with mode pair (1, 2) and mode pair (3, 4), for the AR = 2, 30° minor-plane inclined-B elliptical jet, colored by the local axial velocity. (a) t/T = 0.0. (b) t/T = 0.0625. (c) t/T = 0.125. (d) t/T = 0.1815. (e) t/T = 0.25. (f) t/T = 0.3125. (g) t/T = 0.3750. (h) t/T = 0.4375. (i) presents the 3-D structures, (ii) shows the concerned vortex ring pair structure.

Figure 16

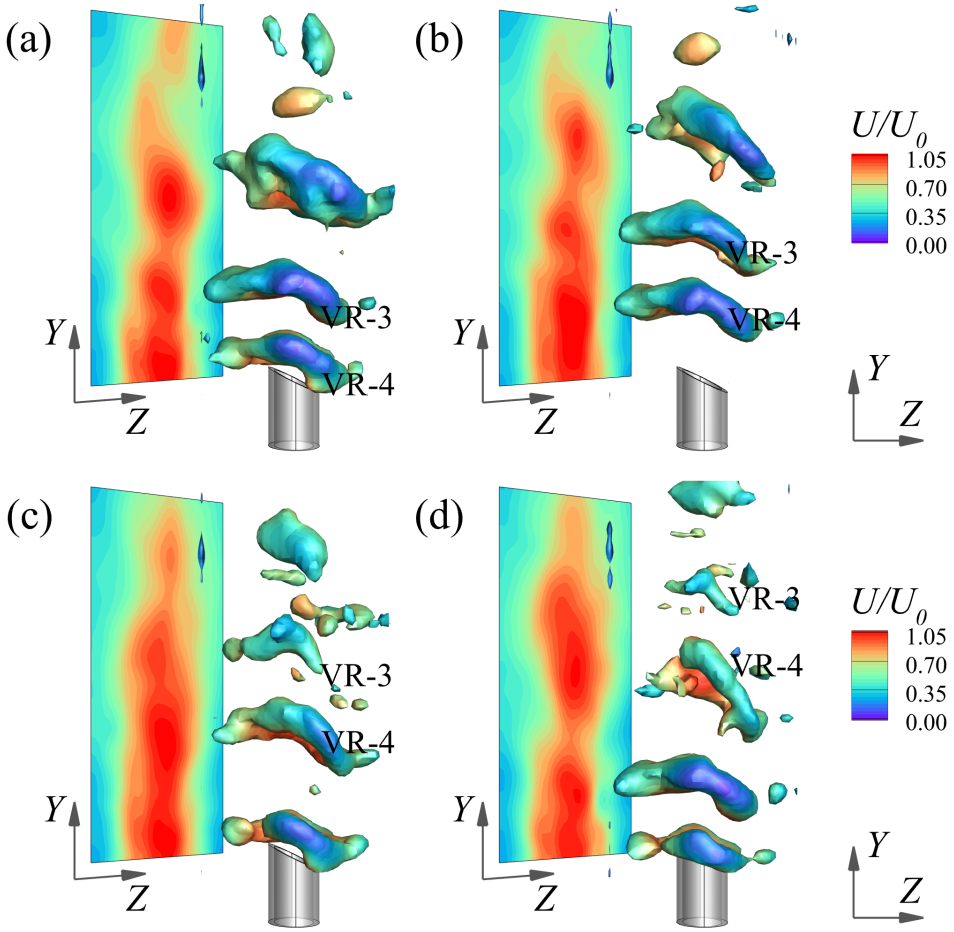

Evolution of unmerged vortex ringsVR-3 and VR-4 reconstructed with mode pair (1, 2) and mode pair (3, 4), for the AR = 2, 30° minor-plane inclined-B elliptical jet, colored by the local axial velocity. (a) $t/T = 0.3750$. (b) $t/T = 0.5833$. (a) $t/T = 0.7917$. (b) $t/T = 1.00$. (i) presents the 3-D structures, (ii) shows the concerned vortex ring pair structure.

Figure 17

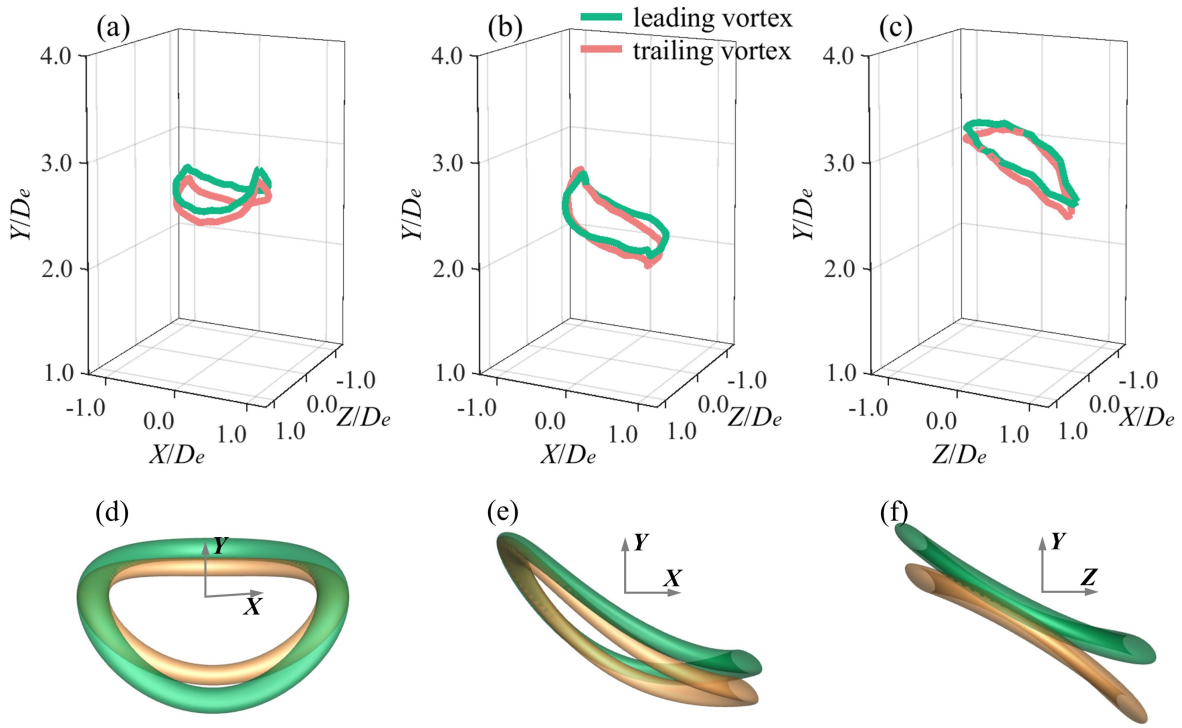

Statistical results and topology of vortex ring merging for different types of elliptical jets. (a, d) Elliptical jet with AR = 2, (b, e) major-plane inclined-A elliptical jet, (c, f) Minor-plane inclined-B elliptical jet

Figure 18

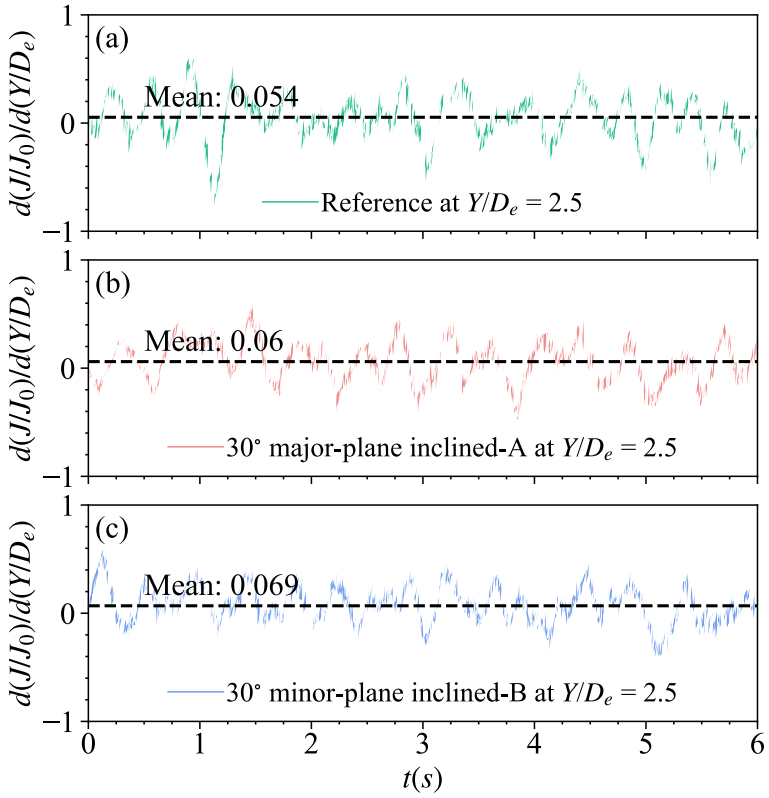

Instantaneous entrainment rate variation for elliptical and inclined elliptical jets at Y/D_e = 2.5, r/D_e = 1.25, (a) Elliptical jet with AR = 2, (b) Major-plane inclined-A, (c) Minor-plane inclined-B

Figure 19

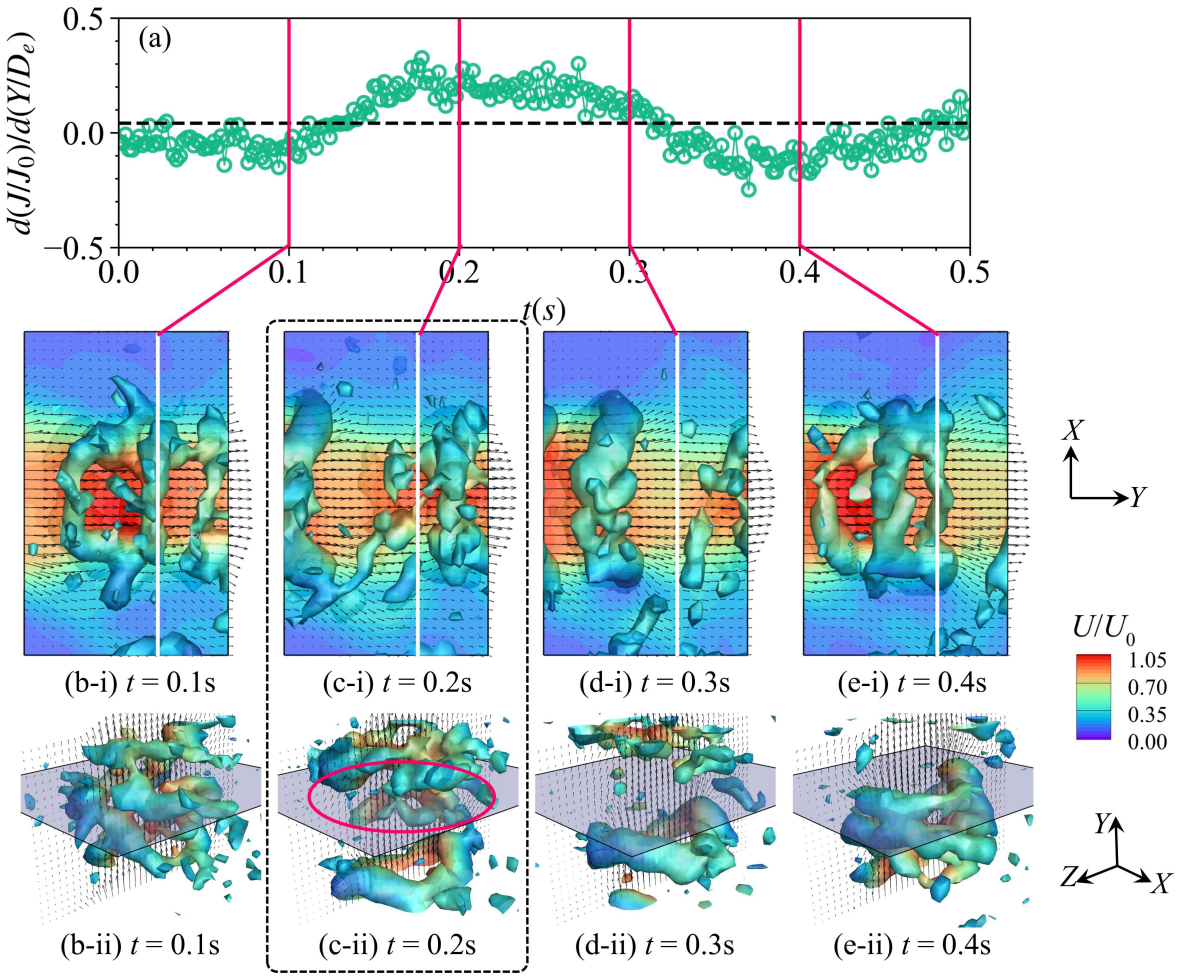

Temporal evolutions of the entrainment rate versus K–H vortex ring structures passing the plane of Y/D_e = 2.5, for non-inclined elliptical jet of AR = 2.

Figure 20

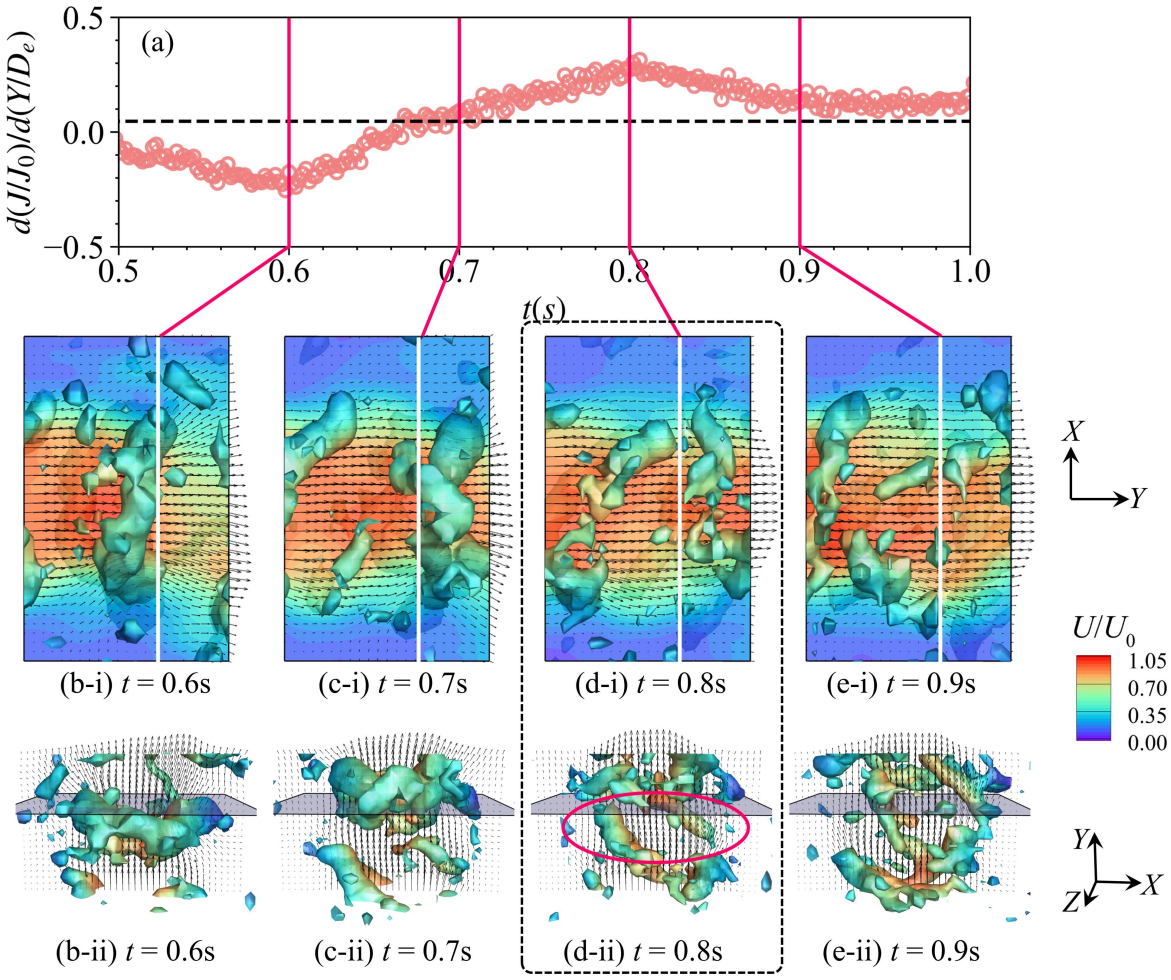

Temporal evolutions of the entrainment rate versus K–H vortex ring structures passing the plane of Y/D_e = 2.5, for major-plane inclined-A elliptical jet.

Figure 21

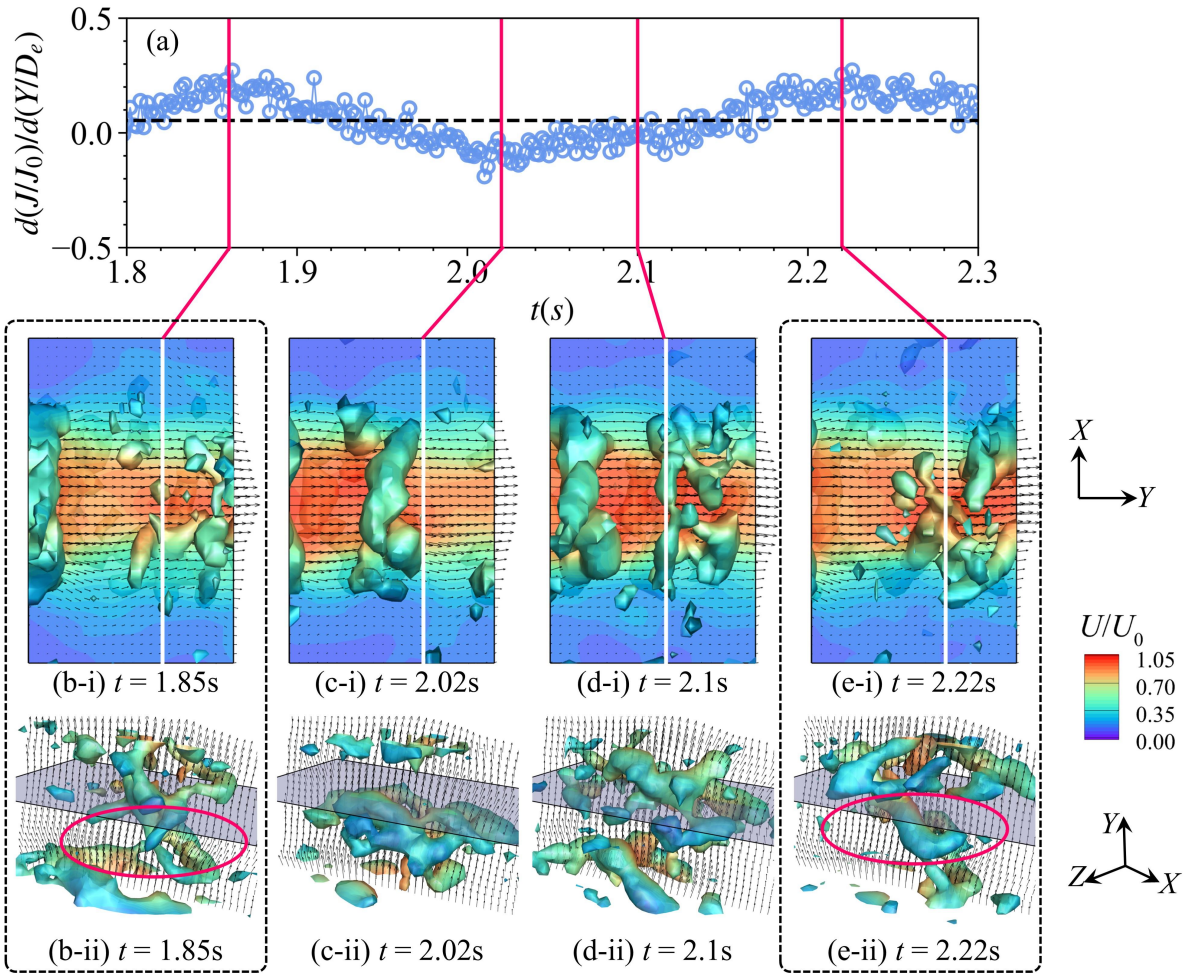

Temporal evolutions of the entrainment rate versus K–H vortex ring structures passing the plane of Y/D_e = 2.5, for minor-plane inclined-B elliptical jet.